Towards clinically useful coded apertures for planar nuclear medicine imaging

David Mark Starfield

A thesis submitted to the Faculty of Engineering and the Built Environment, University of the Witwatersrand, Johannesburg, in fulfilment of the requirements for the degree of Doctor of Philosophy.

Johannesburg, 2009

Declaration

I declare that this thesis is my own, unaided work, other than where specifically acknowledged. It is being submitted for the degree of Doctor of Philosophy at the University of the Witwatersrand, Johannesburg. It has not been submitted before for any degree or examination in any other university.

Signed this ______ day of ________________ 2009

____

David Mark Starfield

Abstract

Coded apertures have the potential to increase imaging efficiency in nuclear medicine without degrading resolution, but near-field artifacts are present even under idealised aperture and imaging conditions. The purpose of this work is to reduce artifacts prior to reconstruction, and to work towards coded apertures that are clinically useful. A ray-tracing simulator was developed. Far-field conditions produce near-perfect images, but the simulation of distributed sources under idealised near-field conditions results in the presence of artifacts.

Three core concepts are introduced in this thesis: a novel rotatable array of identical limited-field-of-view coded apertures; the use of high-resolution aperture projections; and the deliberate and counter-intuitive use of thin, highly transparent aperture material.

An array of identical limited-field-of-view coded apertures, which can be rotated so as to implement an existing artifact-reduction technique, was simulated. The artifacts that exist for a single coded aperture under idealised conditions are removed. This novel technique remains effective when realistic near-field conditions are introduced into the simulation. However, realistic apertures increase artifacts due to finite pinhole widths and finite thickness of the aperture material. To address the pinhole width problem, high-resolution patterns, in which the smallest hole corresponds to a projection area of 1×1 detector pixels, offer the best trade-off between efficiency and resolution despite the partial volume effect. The finite aperture thickness problem is addressed by another novel concept; viz. the deliberate reduction in material thickness, which results in a highly transparent coded aperture. Simulation shows that this counter-intuitive approach diminishes collimation effects.

The implementation of any or all of these three core concepts, however, reduces count statistics. An ultra-near-field geometry, which would ordinarily result in severe artifacts, can theoretically be used to maintain count statistics, without altering either patient dose or image acquisition time. This was verified by simulation.

A prior-state-of-the-art 1 mm thick tungsten coded aperture, and a deliberately highly transparent 100 μm tungsten foil coded aperture, were constructed for use with a dual head gamma camera. Phantom studies of Technetium-99m point, line, syringe and printed distributed sources were performed. The experimental acquisitions verified the simulation results, for both the prior-state-of-the-art coded aperture and the novel high-transparency coded aperture.

The results and arguments presented in this thesis point to the potential for these three core developments to produce high-quality coded aperture images in a fraction of the time that is taken for a collimator acquisition. The limiting factor appears to be the poor count statistics that result from the low sensitivity of current gamma cameras; a situation which looks set to change given current research trends.

Acknowledgements

This work was carried out under the auspices of the Biomedical Engineering Research Group, within the School of Electrical and Information Engineering at the University of the Witwatersrand, Johannesburg. The work was financially supported in part by the School, by the University, and by the National Research Foundation of South Africa.

The author would like to thank:

> Professors David Rubin and Tshilidzi Marwala, as research supervisors, for the initial conception of this work (had we but known!), for their insight and patient guidance, for assistance with experimental acquisition, and for the coordination of funds.
>
> The Wits Donald Gordon Medical Centre, for use of the Philips Axis gamma camera.
>
> JJ van Dongen, Ian Robus, Jacques Schep, Vincent le Roux and staff of Philips Medical Systems, for the donation of a 'retired' Philips Axis collimator, and for assistance and technical expertise relating to the gamma camera used.
>
> Eric Rood of C E Engineering, for his practical advice, and for assistance with the design and his highly-skilled construction of the gamma camera frame.
>
> Jan Koster and Johan Steyn of the National Laser Centre at the Council for Scientific and Industrial Research, for their expertise in the experimental and final laser drilling and laser ablation of the coded apertures.
>
> Peter Dockerty, Harry Fellows and staff of the Genmin Laboratory, within the School of Electrical and Information Engineering, for technical assistance with coded aperture and gamma camera frame detail, and for phantom-holder construction.
>
> Alex De Bonis of the Hillbrow Hospital, for the loan of alignment apparatus.

Professor Hanlie du Raan and Johan van Staden of the Department of Medical Physics at the University of the Free State, for an introduction to printed phantoms.

Nico van der Merwe of the Medical Physics Department at the Johannesburg Hospital, for assistance with flood phantom preparation.

Professor Rex Keddy of the School of Physics, for his advice and interest, and for assistance with phantom preparation and all experimental acquisitions.

René Mosley of Nuclear Medicine at the Wits Donald Gordon Medical Centre, for her kind and patient assistance with all gamma camera operation.

Dr. Nico Malan of the Department of Nuclear Medicine at the Johannesburg Hospital, for assistance with image transfer.

Professors Jan Esser and Willie Vangu of Nuclear Medicine at the Wits Donald Gordon Medical Centre, for their assistance and interest.

The Centre for Telecommunications Access and Services, within the School of Electrical and Information Engineering, for the loan of additional processing power.

Blake McLuckie, for his design and implementation of a high-speed ray-tracing computer simulator, which was at least 100× faster than the MATLAB-based counterpart.

Barry, Linda and Richard Starfield, for their continued patience, assistance and support, not least with respect to the acquisition and transport of apparatus, and with the proof-reading of papers and of manuscripts.

The students and staff of the School of Electrical and Information Engineering, for their friendship, advice and support.

All those not mentioned above, who discussed the problems and concepts associated with coded apertures, and the many visitors to the lab who inexplicably showed an interest in this work.

Contents

Chapters

Appendices

List of Figures

List of Tables

List of Symbols

The principal symbols used in this thesis are summarised below, each providing a reference to the equation in which it is first used:

R	the recorded image	Eq. (A.1)
O	the object	Eq. (A.1)
A	the aperture	Eq. (A.1)
$\ast$	convolution	Eq. (A.1)
O'	the reconstructed image	Eq. (A.2)
G	the decoding array	Eq. (A.2)
$\otimes$	correlation with periodic conditions	Eq. (A.2)
δ	an impulse or delta function	Eq. (A.4)
E	electromagnetic energy	Eq. (A.6)
h_γ	Planck's constant	Eq. (A.6)
f_γ	frequency	Eq. (A.6)
c_γ	speed of light in a vacuum	Eq. (A.7)
λ	wavelength	Eq. (A.7)
i	MURA pattern row	Eq. (A.8)
j	MURA pattern column	Eq. (A.8)
C_q	the general Jacobi Symbol	Eq. (A.8)
s	'basic' MURA pattern size	Eq. (A.9)
c	detector pixel horizontal distance from aperture centre	Eq. (A.10)
d	point of source horizontal distance from aperture centre	Eq. (A.10)
h_1	height of source above aperture	Eq. (A.10)
h_2	height of aperture above detector	Eq. (A.10)
r	physical point of source distance from detector pixel	Eq. (A.11)

I_c	corrected activity	Eq. (A.12)
I_m	measured activity	Eq. (A.12)
α	angle of incidence relative to the system axis	Eq. (A.14)
e	root-mean-square error	Eq. (A.17)
O_q	phantom image intensity at pixel q	Eq. (A.17)
$O_q^{'}$	reconstructed image intensity at pixel q	Eq. (A.17)
R_r	the recorded image for a rotated aperture	Eq. (A.18)
A_r	the rotated aperture	Eq. (A.18)
$O_r^{'}$	the reconstructed image for a rotated aperture	Eq. (A.19)
G_r	the decoding array for a rotated aperture	Eq. (A.19)
k	ideal PSF	Eq. (A.22)
l	projected PSF	Eq. (A.22)
m	correction factor	Eq. (A.22)
$\mathcal{F}$	Fourier transform	Eq. (A.23)
M	transfer function	Eq. (A.24)
$\mathcal{F}^{-1}$	inverse Fourier transform	Eq. (A.25)
I_S	intensity at a point source S	Eq. (A.26)
r_q	a general distance away from a point source S	Eq. (A.26)
I_q	intensity of a point source S at r_q	Eq. (A.26)
r_x	shortest distance between source and detector	Eq. (A.27)
r_y	longest possible distance between source and detector	Eq. (A.28)
h	height of the source above the detector	Eq. (A.28)
w	length of side of a square detector	Eq. (A.28)
ΔI	maximum change in I_q on the detector	Eq. (A.30)
t	aperture material transmission	Eq. (A.32)
ρ	aperture material density	Eq. (A.32)
μ	aperture material attenuation coefficient	Eq. (A.32)
r_m	effective thickness of the aperture material	Eq. (A.32)
x	aperture material thickness	Eq. (A.36)
w_p	'pinhole' width	Eq. (A.36)
a	aperture material attenuation	Eq. (A.40)

N	normally distributed random number	Eq. (A.41)
$\Delta I'$	change in activity at the detector	Eq. (A.42)
n_a	number of individual apertures in an array	Eq. (A.42)
f_1	open fraction of a self-supporting pattern	Eq. (A.42)
f_2	open fraction of a non-self-supporting pattern	Eq. (A.42)
a_1	highly transparent aperture material attenuation	Eq. (A.42)
a_2	opaque aperture material attenuation	Eq. (A.42)
Δb	change in acquisition bit-depth	Eq. (A.43)
y	physical aperture length of side	Eq. (A.45)
y_m	maximum physical aperture length of side	Eq. (A.45)
s_m	maximum ‘basic’ MURA pattern size	Eq. (A.45)

Nomenclature

2D two-dimensional

3D three-dimensional

‘basic’ MURA, which is the core pattern prior to the mosaic

CA coded aperture

CM coded mask

EMBS Engineering in Medicine and Biology Society

FOV field of view

IEEE Institute of Electrical and Electronics Engineers

IFMBE International Federation for Medical and Biological Engineering

LEHR low-energy high-resolution

MLEM maximum-likelihood expectation-maximisation

MURA modified uniformly redundant array

NRA non-redundant array

NTHT no two holes touching

‘pinhole’, which as opposed to a true pinhole is of finite area

PSF point spread function

RMA radiation modulation aperture

RMSE root-mean-square error

SNR signal-to-noise ratio

^{99m}Tc radioisotope Technetium-99m

URA uniformly redundant array

Preface

Prior to reading this thesis, the reader is advised to acquire a copious quantity of bookmarks, along with scrap parchment, ink and quill. Further requirements are a comfortable armchair and a locked door. Last but certainly not least, and failing all of the above: a receptive mind.

Chapter 1

Introduction

1.1 Nuclear medicine

In diagnostic nuclear medicine, a radioactive tracer is introduced into the patient [1]. The ‘labelled’ compound can then be imaged by a gamma camera. As very small concentrations of radioactivity can be detected, nuclear medicine provides high-sensitivity information relating to biological function [1], at concentration levels that are not provided by less invasive imaging modalities.

1.2 Image formation

The pinhole camera was first introduced for the purposes of optical imaging, and has a resolution that is proportional to the area of the pinhole. An infinitely small pinhole would in theory attain perfect resolution [2], but would allow infinitely little light through to the detector.

A lens can transmit more light than a pinhole, and allows the image to be focused. While suitable for a wide range of photon energies, the technique is not practical at higher energies. X-ray radiation can, for example, only be focused by means of grazing incidence reflection at energies below 10 keV [3].

Collimators consist of septa that are designed to attenuate radiation [1]. For example, a parallel-hole collimator only allows gamma-rays that are nearly coaxial with the system axis to illuminate the gamma camera. A collimator is illuminated by an isotropic point source of radiation S (figure 1.1). As with pinhole cameras,

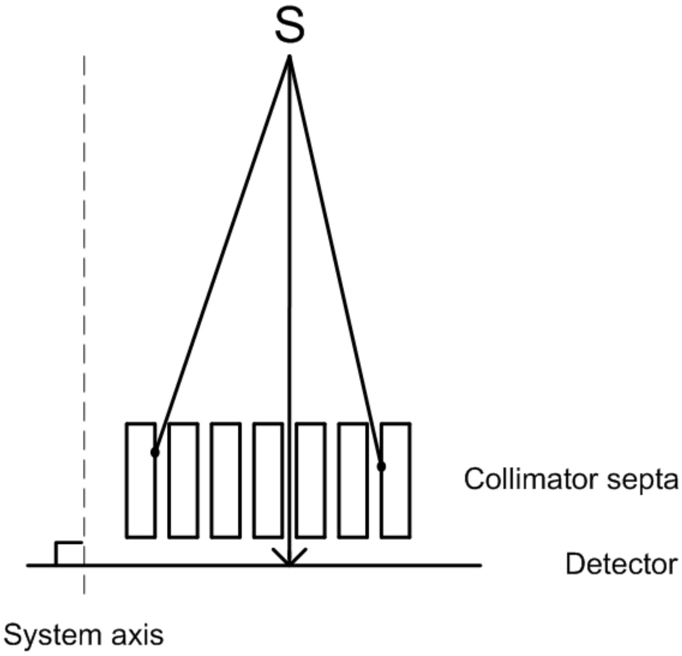

Figure 1.1: Schematic of a parallel-hole collimator

collimators are limited by an inherent trade-off: resolution can only be improved at the cost of efficiency [1], as septal width must remain fixed if the radiation is to be attenuated.

The coded aperture (CA), also known as a coded mask (CM) or as a radiation modulation aperture (RMA), has numerous 'pinholes' (which as opposed to true pinholes are of finite area), arrayed so that the source is multiplexed but in a pattern that allows for a unique reconstruction [2]. Multiple holes increase the open fraction of the aperture without the degradation of resolution [4].

Note that 'pinholes' in inverted commas refer to realistic pinholes. This is in contrast to idealised true pinholes without inverted commas, which are infinitely small, and as such represent a mathematical abstraction.

Coded apertures have the potential to increase the signal-to-noise ratio (SNR) of the system [5]. An increased SNR can theoretically be manipulated to improve image resolution, to shorten imaging time, or to reduce the patient's dose of radioactivity [2] – any one of which provides sufficient motivation for further investigation.

1.3 Thesis layout

This thesis begins with a review of basic coded aperture theory, following which the theoretical concepts are tested by means of idealised simulation. Consecutive sections then incrementally introduce more realistic features, so as to allow for the independent examination of each non-ideal factor in turn.

Chapter 2 summarises both the basic theory and the existing literature, and leads to the problem statement and research goals of chapter 3. Chapter 4 revisits and tests the basic theory by means of idealised simulation. Chapter 5 presents the contributing theory, which aims to address the primary causes of the artifacts that are associated with the real world's dismal lack of ideality. Chapter 6 describes the experimental apparatus, acquisition protocol and phantom studies. Lastly, chapter 7 summarises the concepts that are introduced in this thesis, and suggests potential avenues for future work.

In order to maintain the continuity of the text, mathematical detail is presented in appendix A, while additional schematics and simulated images may be found in appendices B and C respectively. Photographs relating the experimental apparatus are presented in appendix D. Tabular data and a comparison of the features of the primary simulated images may be found in appendix E. Finally, appendix F provides a list of the publications that have been derived from this work at the time of writing.

Chapter 2

Coded apertures

2.1 Far-field conditions

Coded apertures have historically been used in astrophysics, to image distant cosmic sources [6, 7, 8, 9]. This is a far-field geometry and gamma-rays that originate from the same point source can, on approach to the aperture, be considered parallel [2]. Parallel rays originate from a far-field isotropic point source S (figure 2.1).

All 'pinholes' of the aperture cast projections of the source onto the detector, and the multiple projections overlap. With respect to image reconstruction, another perspective is useful, namely that all points of the source cast projections of the coded aperture pattern onto the detector [2, 10]. The multiple patterns overlap, but each known pattern is shifted and weighted according to the location and activity of each specific point source.

Under ideal conditions, image acquisition is modelled by convolution of the source with the coded aperture pattern. (Note that correlation is identical to convolution with a reflection [11].) Correlation of the result with the same binary coded aperture pattern achieves a unique reconstruction – provided that the autocorrelation function of the aperture pattern is an impulse or delta function [5, 12] (appendix A.1, page 66). A single point source then reconstructs as a peak, and all other positions reconstruct equally as a constant background [5].

Note that the use of non-overlapping images would require a larger detector, which would increase background noise [4]. A pattern that has an open fraction of 50 %, for example, does actually use the entire detector as the opaque percentage

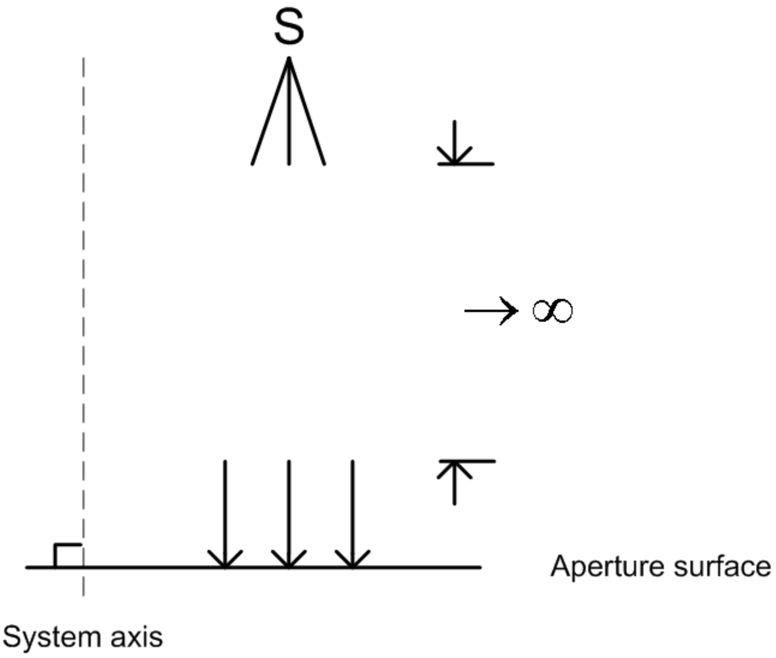

Figure 2.1: Schematic of parallel rays on approach to the aperture

of the pattern allows for measurement of the background [4, 8]. Further, a ray approximation is valid for gamma-rays, as the wavelength is likely to be far smaller than the 'pinhole' size (appendix A.2, page 67).

2.2 Aperture patterns

There are multiple families of aperture patterns. Fresnel zone plate and random 'pinhole' patterns have peak-to-sidelobe ratios that are non-ideal [9].

An improved autocorrelation function is obtained if the binary patterns are derived from difference sets [9, 12]. Planar difference sets are related to the Golomb ruler, a mathematical concept in which the 'space' between any two 'marks' on the ruler is unique [9, 13]. This is a special case of cyclic difference sets, in which the number of times a particular 'space' occurs between any two 'marks' on the ruler must be the same for all 'spacings' [9, 13].

The non-redundant array (NRA) and the uniformly redundant array (URA) are constructed from planar and cyclic difference sets respectively [5, 9]. The modified URA (MURA) [11], and self-supporting MURA arrays with no two holes touching (NTHT) [14, 15, 16], have mathematical properties similar to those of the URA but are no longer classified as being cyclic difference sets [11].

A square MURA is generated from a prime number, and the elements are pattern-centred [11, 17]. Repetition of the core pattern gives a mosaic [11]. (Further detail is provided in section 4.1, page 14.) The resultant MURA is either symmetric about the centre [11], or is anti-symmetric, with the property that rotation by 90 ° inverts the aperture pattern [18, 19].

2.3 Near-field conditions

In nuclear medicine diagnostics, the patient is positioned as close to the gamma camera as is possible. This allows the maximum number of counts of radioactivity to be recorded, but near-field artifacts result [10, 18].

The mathematical expression for near-field artifacts contains three terms of significance [18]. Zero-order artifacts require an estimate of the physical source distance for mathematical correction. (Further detail is provided in section 4.2, page 15.) First-order artifacts require that the centre of mass of the source be centred with respect to the aperture pattern [18].

Second-order artifacts are present as hyperbolic dark and light regions at the borders of the image, and are reduced by the mask anti-mask technique [18], which was first introduced to compensate for mask irregularities in astrophysics [7]. Acquisition takes place with the original aperture pattern. This is followed by acquisition with an inversion of the original aperture pattern, and the two images are summed [7, 18, 20]. Anti-symmetric MURA coded aperture inversion is equivalent to 90 ° rotation [18, 19].

2.4 Imaging geometries

As with pinhole cameras, geometry determines whether a projection of the source undergoes magnification or minification [10]. Imaging geometry also defines the field of view (FOV) of the system.

A point of the source that projects the full aperture pattern onto the detector lies in the fully-coded FOV [9]. A point that lies in the partially-coded FOV projects a

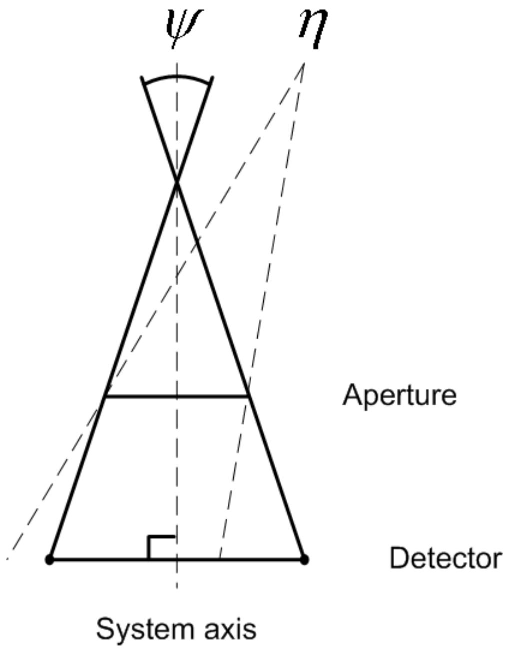

Figure 2.2: Schematic of the fully-coded and partially-coded fields of view

portion of the necessary pattern, and cannot be reconstructed correctly [9]. ψ is the fully-coded FOV (figure 2.2). η lies in the partially-coded FOV and projects only a portion of the aperture pattern onto the detector.

A box camera with an aperture and detector of equal size, for example, only has a fully-coded FOV at the point of intersection of the system axis and infinity [9]. A box camera is illuminated by an isotropic point source of radiation S (appendix figure B.1, page 90). Note that η again lies in the partially-coded FOV.

Cyclic patterns require the projection of a single cycle of the aperture pattern, that is, one period of the mosaic [5, 9]. A box camera with a mosaic aperture and detector of equal size can, by comparison, have a fully-coded FOV that at a 1:1 imaging ratio is equal to the size of the detector. A single cycle of a mosaic aperture illuminates the full detector (appendix figure B.2, page 91). A different cycle of the same aperture overlaps that of appendix figure B.2 (appendix figure B.3). Combination of appendix figures B.2 and B.3 demonstrates the overlap of mosaic aperture cycles (figure 2.3). Note that the fully-coded FOV ψ is equal in size to both the mosaic aperture and the detector.

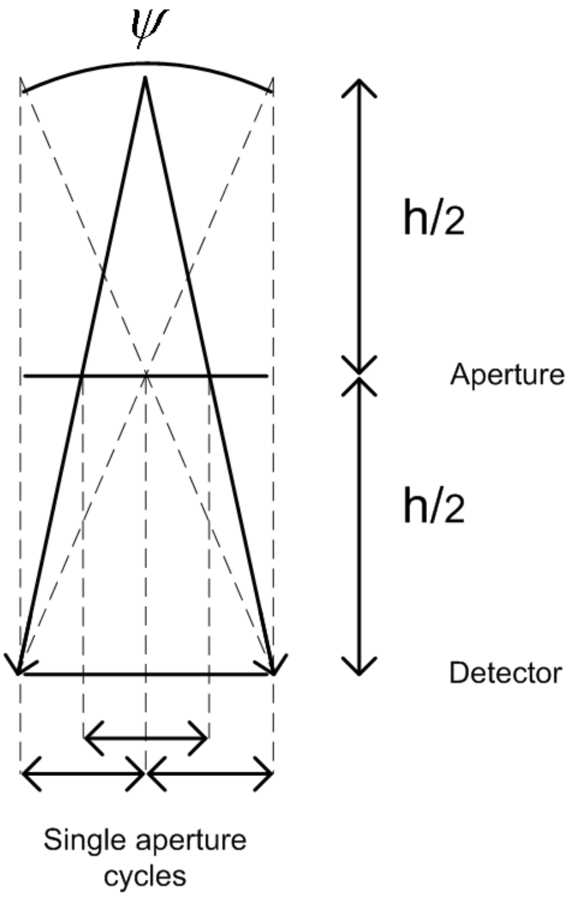

Figure 2.3: Schematic of the overlap of mosaic aperture cycles

2.5 Laminography

The magnification or minification of the projected aperture pattern is unique to the specific depth of the source [10]. (Further detail is provided in section 4.4.1, page 19.) Slices at multiple depths can then be reconstructed from a single coded aperture image [10, 21], if the decoding array is scaled to match the unique size of the projected data for each specific depth.

The axial resolution of the tomographic reconstruction therefore varies with the distance of the source, as it depends on changes in the size of the projected data [10]. A shorter source to aperture distance increases the severity of near-field artifacts, but does improve axial resolution [10].

Data at any depth other than that of reconstruction results in the presence of structured artifacts [2, 10]. By contrast, collimators require multiple views for the reconstruction of a three-dimensional (3D) object, but the data is refined with each additional measurement. Clear coded aperture images of planar sources must be obtained prior to consideration of the 3D realm, which lies beyond the scope of this thesis.

2.6 Literature survey

A doctoral thesis relating to coded aperture imaging was submitted by Accorsi at the Massachusetts Institute of Technology in 2001 [22]. As the Accorsi thesis provides a comprehensive review of the history and development of coded aperture imaging, this thesis does not duplicate that review. Rather, a number of contributions to the field both prior and subsequent to the Accorsi thesis are highlighted.

2.6.1 Classic work

Calabro and Wolf discussed the mathematical synthesis of two-dimensional (2D) binary arrays that exhibit 'desirable correlation properties' in 1968 [17]. This theoretical work provided a foundation for the multiple families of coded aperture patterns that were to follow.

Barrett imaged a nuclear medicine thyroid phantom using a Fresnel zone plate in 1972 [21], and in 1978 Fenimore concluded that the SNR of a coded aperture system depends on the nature of the source [5]. Steinbach and Macovski then detailed the point spread function (PSF) of a coded aperture system in 1979 [23].

In the same year, Cannon and Fenimore published classic tomographic experiments using URA systems [10]. Near-field artifacts were discussed with clarity, as was the trade-off between the presence of near-field artifacts and the ability to obtain a high tomographic resolution [10]. Fenimore developed a modulation transfer function for URA systems in 1980 [14], and Fenimore and Cannon examined the effect that the reconstruction method has on image resolution in 1981 [15].

2.6.2 Artifact reduction

McConnell and Forrest suggested the mask anti-mask procedure for an astrophysical application in 1982 [7], while Cook and Finger discussed the rotation of anti-symmetric hexagonal URA patterns in 1984 [8]. These concepts form the basis of the current technique for the reduction of second-order near-field artifacts [18, 19, 20].

An extensive discussion was published by Caroli and Stephen in 1987 [9]. It incorporated the coded aperture patterns that were available, fully-coded and partially-coded fields of view, and imaging geometries in astronomy. Dunphy and McConnell mentioned the difficulties associated with implementing the mask anti-mask technique on a balloon-borne coded aperture telescope in 1989 [24].

In the same year, Gottesman and Fenimore published their discovery of MURA coded aperture patterns [11], based on the 1968 binary array work of Calabro and Wolf [17]. The advent of the MURA led to a significant increase in the number of patterns that are available for coded aperture design [11]. The paper also discussed pattern centring by means of cyclic permutation of the array [11].

The rise of personal computing coincided with an increase in computationally intensive work. Rogulski and Barber simulated the use of coded apertures in high-resolution tomographic imaging in 1993 [25], and Berrim and Lansiart published the use of a maximum-likelihood expectation-maximisation (MLEM) algorithm in the reconstruction of 3D coded aperture images in 1996 [26]. Liu and Rangarajan evaluated a dual-head camera system in 1998, in which a collimator and a coded aperture acquired images simultaneously [27].

2.6.3 The Accorsi thesis

Completion of the Accorsi thesis in 2001 [22] corresponded to the publication of multiple papers. Accorsi and Gasparini provided an analysis of the coded aperture patterns that are optimal for nuclear medicine [16], and in a separate paper presented experimental results for a 1.5 mm thick tungsten coded aperture with holes of width 1.11 mm, and an FOV of 9 cm × 9 cm [2].

Accorsi and Lanza also detailed the expansion of the mathematical expression for near-field artifacts in 2001, so as to obtain the zero-order, first-order and second-order terms [18]. The paper suggested use of the mask anti-mask technique in nuclear medicine – a concept that was independently suggested by Vassilieva and Chaney [20].

It may be of interest to note that while the Accorsi paper was submitted in December 2000, the Vassilieva paper was submitted to the same journal in February 2001. The papers were published in September 2001 and in March 2002, respectively. The filing of provisional patents may be of greater interest: Accorsi and Lanza filed in September 2000 [28], but Vassilieva and Chaney filed 10 months earlier in November 1999 [29].

The Vassilieva and Chaney paper [20] noted that success, relating to the tomographic work of Cannon and Fenimore in 1979 [10], had in 20 years not yet been achieved. In the preface to his thesis of 2002, Chamberlain likened coded apertures to ‘cold fusion’: promising but beyond reach [30].

2.6.4 Gamma-ray microscopy

Accorsi and Lanza discussed the use of a dual-head camera system in 2003 [31], but as opposed to the 1998 work of Liu and Rangarajan [27], the mask and the anti-mask acquire images simultaneously. Gmar and Gal acquired images using hexagonal coded apertures with a compact gamma camera in 2004 [32]. In the same year, Accorsi and Autiero presented a coded aperture gamma microscope, in which a 75 μm thick tungsten coded aperture has holes of width 70 μm for use at 22 keV [33].

Mu and Liu found that an MLEM reconstruction approach may not require use of the mask anti-mask technique in 2006 [34], and Alnafea and Wells suggested that near-field artifacts can be predicted and corrected [35]. Chen applied the concept of simulated annealing to coded aperture imaging in 2007 [36], and Lang and Liu used global optimization techniques to suggest new NRA and URA patterns [37, 38].

Accorsi and Celentano published the results of imaging a mouse thyroid in February 2008 [39], using a 100 μm thick version of the 70 μm hole coded aperture initially reported in the Accorsi and Autiero paper of 2004 [33]. One month later, Miller and Barrett published results for a coded aperture that was designed to take advantage of the high intrinsic resolution of a ‘bazooka’ gamma-ray microscope [40]. The 25 μm thick platinum coded aperture has 684 holes of width 25 μm, forming a pattern of size 0.95 mm $\times$ 0.95 mm, also for use at approximately 22 keV.

Note that work on this thesis was initiated in 2004. The problem statement that follows is, therefore, based on the literature that was available at that time. The most recent contributions to the field have, however, been included for completeness and the concepts are revisited in subsequent chapters.

Chapter 3

Problem statement

3.1 Perspective

There is an SNR advantage for coded apertures that image distant point sources [5]. However, artifacts are prevalent under near-field conditions [10] and the SNR deteriorates further for distributed sources [5]. The SNR advantage can exist under near-field conditions, but it is with the constraint that source activity be spread over a small number of pixels [5, 16, 19]. Advances developed for near-field imaging conditions [18, 20] do not alter this result [19], and coded apertures are not used in general purpose nuclear medicine. That is, the FOV and performance of coded apertures is not clinically useful.

3.2 Purpose

The low-energy high-resolution (LEHR) parallel-hole collimator is used most frequently in nuclear medicine diagnostics [1]. The purpose of this work is firstly to allow for a direct comparison of general purpose coded aperture and LEHR collimator imaging.

Secondly, the aim is to find the conditions under which a near-perfect near-field reconstruction can be attained, if such conditions exist, and to then develop novel coded aperture imaging methodologies. Acquisition should be such that near-field artifacts are already reduced prior to reconstruction, relative to the prior state of the art. This must be at a near-field geometry in which artifacts would otherwise be present.

3.3 Reasoning

Coded apertures may still be considered despite the presence of artifacts, if faster imaging times can be achieved. The apertures are clearly more likely to be implemented if the images are artifact-free. If it is possible to solve the problem at geometries in which artifacts exist, the possibility of tomography is not excluded.

The mathematical derivation of the SNR is of necessity based on assumptions. The derivation must be dependent on the chosen imaging geometry, aperture pattern family, physical aperture properties, as well as artifact-reduction and image-reconstruction techniques.

Gamma cameras are typically fitted with exchangeable collimators, which allows coded apertures to be mounted without gamma camera alteration. The apertures must be used in the same manner as collimators if they are to be widely applicable, and if they are to be directly comparable to LEHR collimators.

That is, the activity of the source must be appropriate and the source must be positioned as close to the gamma camera as is possible. The image must be acquired over a wide FOV, and as with parallel-hole collimation, the size of the projection must be equal to the size of the source.

If a coded aperture is positioned halfway between the detector and the source, a 1:1 imaging ratio is obtained. A box camera with a detector and a mosaic cyclic aperture of equal size then makes the most efficient use of the FOV.

Chapter 4

An ideal world

4.1 Convolution

Coded aperture theory is defined for far-field 2D noise-free sources [18]. Provided that the autocorrelation function of the aperture pattern is ideal, an ideal image PSF is achieved.

The first test for any coded aperture pattern is then to convolve the pattern with a digital phantom (pixel-based representation of a source), and to perfectly reconstruct that phantom by correlation of the data with the original coded aperture pattern. An MURA is optimal for the purposes of nuclear medicine [16].

A prime number sets the size of the 'basic' square MURA [11]. The binary Jacobi Symbol, which is related to the quadratic residue of the prime [17], is calculated for all pattern elements (appendix A.3, page 68). The elements are shifted so as to be pattern-centred [11], and the basic pattern is then repeated to obtain a mosaic, relative to but excluding the central row and column of the aperture pattern [5, 9]. A prime that generates an anti-symmetric pattern must be chosen if the mask anti-mask technique is to be implemented by means of a 90 ° rotation of the aperture [19].

As a cyclic pattern, a point of the phantom must project a single cycle of the aperture pattern onto the detector [5]. To test convolution, the multiplexed data used for correlation is then equal in size, and centred with respect to the 'basic' aperture pattern. A perfect reconstruction of the digital phantom results (figures 4.1, 4.2 and 4.3). That is, on a pixel-by-pixel basis the images are identical.

A 2D digital Shepp-Logan phantom [41] is used throughout this thesis, as it provides a simplified model of the human brain, with distributed features that range in both scale and intensity. Note that the original model was intended to represent X-ray attenuation. In this thesis, the model is taken as being representative of the emission of gamma-rays, with the white pixels of the skull being indicative of the highest level of radioisotope uptake.

Print quality and settings, together with the paper used to print this thesis, can have a significant effect on the ability to discern fine changes within either the simulated or the acquired images. If features or artifacts prove difficult to discern, referral to digital versions of the images is recommended, as is an appropriate adjustment of the brightness and contrast of the display. (The disc that accompanies this thesis contains image files for all simulations and acquisitions, ordered by figure number.)

4.2 Ideal far-field simulation

The second test is to examine the coded aperture under ideal far-field conditions. Relative to the convolution of the preceding section there is the inclusion of 3D space.

If this is to be the only alteration, a 2D noise-free source and ideal coded aperture are required. The aperture is modelled as infinitely thin, but with opaque elements that completely attenuate gamma-rays, and with transparent elements that act as true pinholes without loss of resolution.

For all points of the source, where each point radiates isotropically, a line is traced through all pinholes of the coded aperture. The point of intersection of each line with the plane of the detector is found. For a given line, the activity at the detector is calculated, based on the activity of and physical distance from the corresponding point source. The complete system is represented as a discrete array of points, as was implicitly the case with convolution, and activity at the detector is interpolated (appendix A.4, page 73).

A geometry is chosen in which the source is substantially further from the aperture than the aperture is from the detector. The reconstruction of the multiplexed data then darkens with the radial distance from the centre of the image (figure 4.4). That is, the pixel intensities decrease relative to the phantom.

Figure 4.1: 2D digital Shepp-Logan phantom

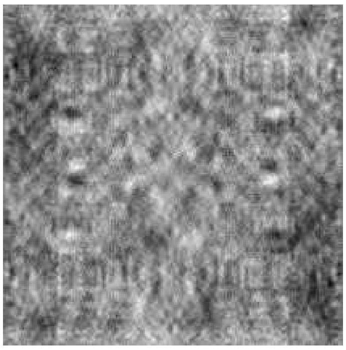

Figure 4.2: Convolution of Shepp-Logan phantom and aperture

Figure 4.3: Perfect reconstruction of the convolved result

Under far-field conditions, the autocorrelation function of the projection of an ideal coded aperture pattern approaches an impulse [10, 12]. That is, the entire aperture pattern approximates a single true pinhole, positioned at the centre of the pattern.

Activity at a given point of the detector can then be corrected for physical distance, as if the coded aperture image had been acquired with that single true pinhole (appendix A.5, page 74). This simple and intuitive correction realizes a perfect reconstruction of the digital phantom (figure 4.5), and is identical to the existing mathematical correction for zero-order artifacts [18] (appendix A.6, page 75).

A comparison of the features of the primary simulated images is provided (appendix table E.2, page 105), together with a full description of the column labels (appendix table E.1). Note that a bullet indicates whether a feature is incorporated in a specific simulation. A root-mean-square error (RMSE) measurement quantifies the results (appendix A.7, page 76), but should only be viewed in the context of the features modelled. (As the table provides a single-page comparison of both simulation features and RMSE measurements, regular referral is recommended.)

4.3 Ideal near-field simulation

The third test is to examine the coded aperture under ideal near-field conditions. Relative to far-field, the only alteration is the use of a 1:1 imaging ratio and the geometry of a box camera (appendix figure B.2, page 91), other than the limitation of space. Note that a source to crystal distance of 20 cm and a 20 cm × 20 cm FOV are simulated throughout, unless stated otherwise. A method for obtaining a more practical FOV is discussed in due course.

The multiplexed data used for correlation is equal in size to the projected 'basic' aperture pattern, and is centred with respect to the coded aperture. Under ideal near-field conditions, the autocorrelation function of the projected aperture pattern is non-ideal [10, 18]. That is, perfect aperture properties no longer give an ideal PSF (appendix figure C.1, page 95).

The single true pinhole approximation correction, or the correction for zero-order artifacts [18], is then no longer intuitive and has little effect (appendix figure C.2.) First-order artifact correction [18] would complicate clinical acquisition, as the centre of mass of the source must be centred with respect to the aperture pattern, and is not applied.

Figure 4.4: Simulated far-field reconstruction

Figure 4.5: Simulated far-field reconstruction with correction

Subtraction of the mask and the anti-mask acquisitions, followed by correlation, is equivalent to the mask anti-mask technique (appendix A.8, page 77). This approach simplifies reconstruction, particularly with respect to laminography: as opposed to two correlations and an addition for each slice of data, the acquisitions can be subtracted once and correlated for each specific depth.

Application of the mask anti-mask technique [7, 18, 20] lessens second-order artifacts. The hyperbolic dark and light regions at the borders of the image are inverted (appendix figures C.1 and C.3), and are removed (figure 4.6). The enhancement is significant, but the reconstruction of the digital phantom is affected by ghosting, the severity of which is related to the physical distance of the source. If a 1:1 imaging ratio is maintained, an increase in source distance decreases the ghosting (figures 4.7 and 4.8). As the simulation parameters are still highly idealised, these artifacts can only be the result of a near-field geometry.

Note that an increase in source distance is impractical, as it affects the ability to minimise patient dose and reduces axial resolution in tomographic reconstruction [10]. While the 3D realm lies beyond the scope of this thesis, the potential for tomographic imaging must not be ignored.

4.4 Software-based correction

4.4.1 Near-field artifact prediction

A non-ideal PSF is obtained for a specific point source, coded aperture, and near-field imaging geometry. The artifacts relative to the ideal PSF are repeatable, and are therefore predictable. The simulated and ideal point source projections differ (appendix figures C.4 and C.5, page 96), as do the respective reconstructions (appendix figures C.6 and C.7). Note that the geometry of the projected pattern remains unaltered, but the intensity is modulated [10], as is particularly evident at the edges of the pattern (appendix figure C.4). The contrast of appendix figure C.6 has been adjusted so as to make the cross-artifact clearly visible. Subtraction of the simulated and ideal reconstructions leaves only the artifact (appendix figure C.8).

The physical distance of the point determines the magnification or minification of the projection [10] (appendix figures C.9 and C.10), and the precise location of the point in the FOV affects the actual pattern cast by the aperture [5] (appendix

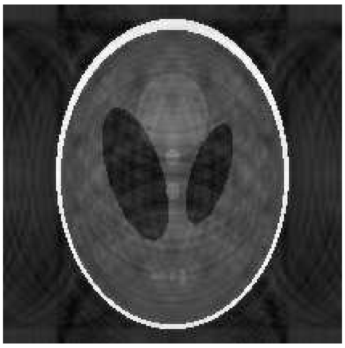

Figure 4.6: Simulated near-field reconstruction with second-order correction

Figure 4.7: Simulated corrected near-field reconstruction at 2× the distance

Figure 4.8: Simulated corrected near-field reconstruction at 4× the distance

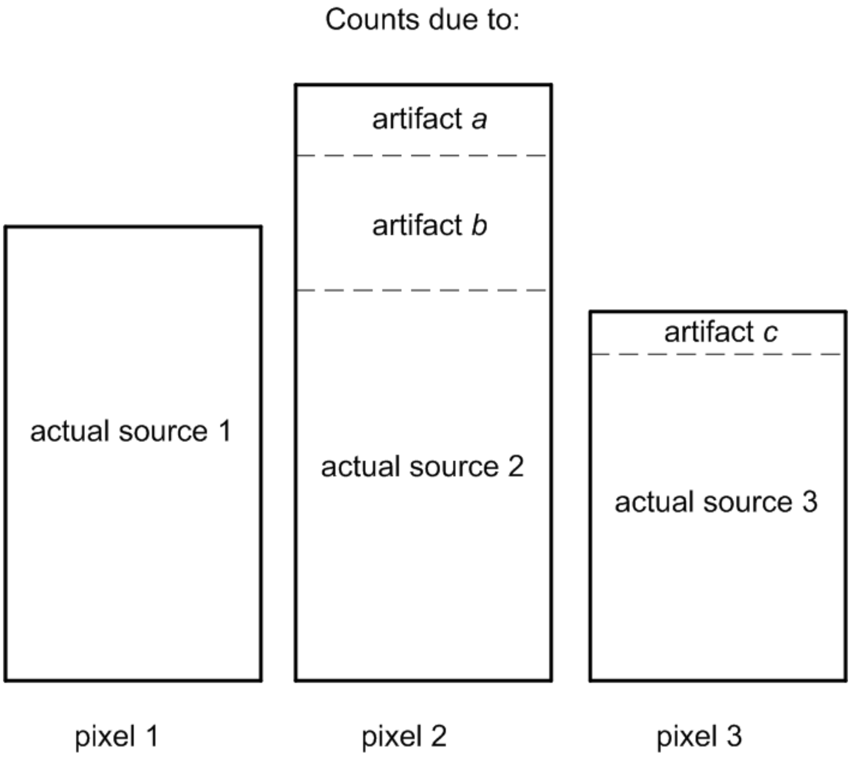

Figure 4.9: Schematic of the composition of reconstructed pixel counts

figure C.11). The symmetry of cyclic patterns assists predictability.

Once the image has been acquired it is not possible to differentiate the object from the artifact. This is a typical inverse problem: the combined data can be calculated from the multiple input signals, but the input signals cannot be calculated from the combined data.

A single reconstructed point can be the summation of a true point and of multiple artifacts (figure 4.9). The artifacts associated with the true point are predictable, but the actual number of reconstructed counts that comprise the true point cannot be known. The artifacts cannot be removed with certainty.

4.4.2 Fourier filters

The non-ideal PSF of the system, relative to the ideal PSF, allows for the calculation of a transfer function in the Fourier domain (appendix A.9, page 78). The transfer function can then be applied to the correction of encoded images as a Fourier filter, within the limited FOV in which the transfer function approximation holds.

4.4.3 ‘Intelligent’ convolution

The decoding procedure can be computed in the spatial as opposed to the Fourier domain. This allows each point of reconstruction to be computed individually, and makes it possible to uniquely correct the encoded data for a given point of reconstruction, without alteration to the data used for the reconstruction of any other point. That is, the encoded data can be corrected to match the expected projection should a point source exist at the point of reconstruction.

This is once more an inverse problem. Knowledge of the acquisition system does allow for software-based correction [35], but the overlap of data makes correction problematic. Note that an iterative-reconstruction approach does have the potential to correct artifacts [26, 27, 42]. The author of this thesis is of the view that, at a fundamental level, software-based correction techniques should only be applied to data that has been acquired in the best possible way.

Chapter 5

Contributing theory

5.1 Coded aperture arrays

5.1.1 Near-field geometries

Perfect aperture properties do not give an ideal PSF under ideal near-field conditions [10, 18, 19]. Relative to the far-field scenario, where the PSF tends toward the ideal, incident gamma-rays due to a point source are not parallel. The distances traversed by gamma-rays differ significantly [10].

If a point source is positioned above a square detector, the shortest distance between the source and the detector is that which is perpendicular to the detector plane. The longest distance to a point of detection, given a box camera, is then from a corner of the detector to a point that is positioned above the diagonally opposite corner. An isotropic point source S illuminates a square detector (appendix figure A.9, page 80).

This simple scenario allows analysis of the maximum change in activity, or intensity at the detector surface due to a single point source. Mathematical expression of this maximum change provides a general equation that can be applied to particular imaging geometries (appendix A.10, page 79). An analysis based on a single point source is highly simplistic, but does provide useful insight.

A range of imaging geometries applied to appendix equation A.31 generates a curve (figure 5.1). ΔI is the maximum change in detector intensities due to a point source S, which is at a height h above a square detector of length of side w. Note that the ratio h/w is used.

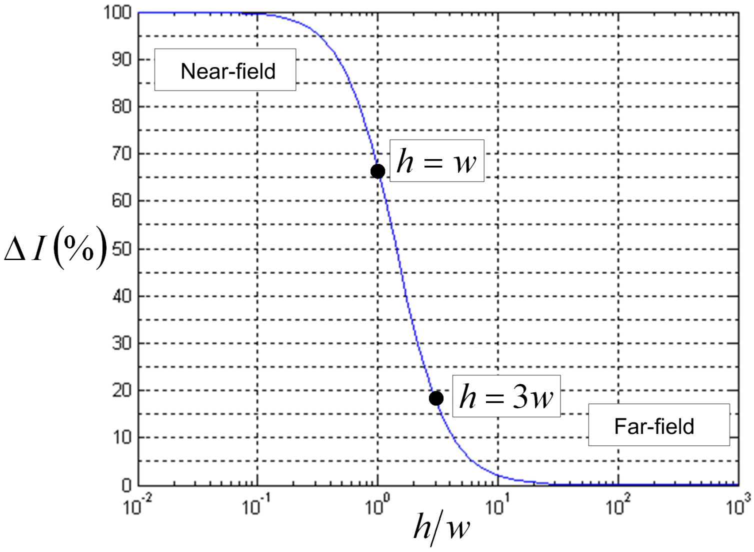

Figure 5.1: Plot of the maximum change in point source detector intensities

5.1.2 A geometric solution

Convolution implies that a point source is imaged equally by each ‘pinhole’ of the coded aperture (appendix A.1, page 66), where the image of the point source falls directly below each ‘pinhole’, without change in intensity. This is a requirement of the decoding procedure [5].

In reality, the change in intensities only tends toward zero under far-field conditions (figure 5.1). At a fixed height above the detector, however, the change in intensities can be manipulated by means of detector size. That is, a limited FOV limits the change in intensities, and can therefore limit near-field artifacts.

From a practical perspective and irrespective of detector size, a radiation attenuation ‘tube’ can be designed to enclose the coded aperture and can extend from the source to the detector. This quasi-collimator can then limit the FOV to a fully-coded unique section of the source, provided that the imaging geometry of a box camera is used (appendix figure B.2, page 91, and figure 2.3, page 8).

An array of multiple identical limited-FOV coded apertures, placed side-by-side in the form of a matrix, allows the overall FOV of the system to remain unaltered. For clarity, only one collimating ‘tube’ is shown (figure 5.2). A 90 ° rotation of each individual coded aperture or element of the matrix is equivalent to a 90 ° rotation of the whole matrix of coded apertures. Individual apertures are marked at top left (appendix figure B.4, page 92). The apertures are individually rotated by 90 °

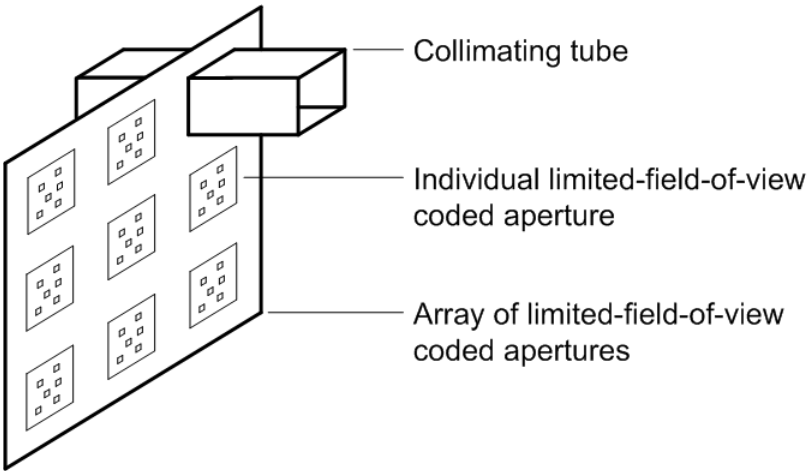

Figure 5.2: Schematic of an array of limited-FOV coded apertures

(appendix figure B.5), and the entire array is rotated by 90 ° (appendix figure B.6). Note that while individual apertures change position, the result is identical to that of appendix figure B.5. The apertures can then be carried on a single sheet of material. (Further detail relating to the mask anti-mask rotation mechanism is provided in section 6.1.1, page 46.)

The existence of an SNR advantage is well established if source activity is spread over a small number of pixels [5, 16, 19]. Further, it can be argued that a reduced angle of incidence is an obvious improvement [2, 10], perhaps achieved with the use of a limited FOV [16]. An array of identical limited-FOV coded apertures, which can be rotated in entirety for second-order artifact reduction is most certainly novel, and is one of the concepts that is introduced in this thesis.

The use of multiple coded apertures has been proposed, with the aim of increasing the FOV so as to reduce scan times [20]. That is, rather than a single coded aperture being moved so as to scan an area larger than the FOV, additional apertures and detectors would increase the FOV, and would therefore accelerate acquisition [20]. By contrast, it is suggested in this thesis that a single coded aperture can be replaced by multiple smaller coded apertures, which taken together cover the same area as the original: a subtle but significant difference.

An array of apertures is advantageous in that it limits the angle of incidence, but maintains the FOV and does allow for implementation of the mask anti-mask technique. Furthermore, the concept controls the degree of multiplexing – particularly with respect to the tomographic reconstruction of 3D sources.

The reduction in sensitivity is discussed in due course, but can be compensated for (section 5.4, page 41.) Note that a 3D source may illuminate more than one coded aperture within the array, but the extent to which this occurs would be determined by the precise geometry of the system, and could be controlled by the geometric design of the 'tubes'.

5.1.3 Ideal limited-field-of-view simulation

Relative to the ideal near-field simulation of a single coded aperture, an array of smaller limited-FOV coded apertures is used. The attenuation 'tubes' are modelled as completely opaque, so that each individual coded aperture images a unique FOV.

A 3×3 array of limited-FOV coded apertures, for example, lessens the ghosting that is associated with near-field artifacts. The classic hyperbolic dark and light regions visible at the borders of each individual aperture image are inverted (figures 5.3 and 5.4), and are removed (figure 5.5). An improved PSF is obtained (relative to figure 4.6, page 20), which approaches that for a single ideal coded aperture under a far-field geometry (figure 4.5, page 18). This result is without the use of either zero-order or first-order artifact correction.

5.1.4 Realistic coded apertures

An ideal coded aperture has been described as being infinitely thin but completely opaque. It is then not possible for a gamma-ray that enters a true pinhole to undergo attenuation.

The simple scenario in which a point source is positioned above a corner of a square detector must now include 'pinhole' width, aperture thickness, and transparency of the aperture material. As was implicitly the case with the ideal coded aperture scenario, it is only meaningful to compare the projection of 'pinholes'.

The shortest distance between the source and the detector is that which is perpendicular to the detector plane, and there can be no attenuation. At the longest possible distance to a point of detection, attenuation becomes a function of the angle of incidence, 'pinhole' width, aperture thickness, and the physical properties of the aperture material. An isotropic point source S illuminates a square detector with

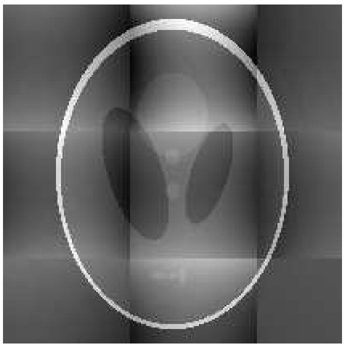

Figure 5.3: Simulated near-field reconstruction, 3 × 3 aperture array

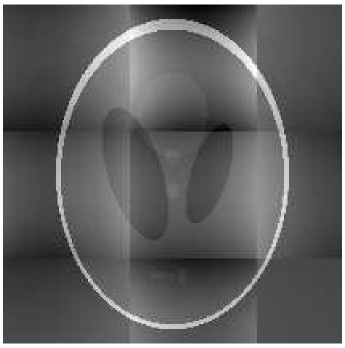

Figure 5.4: Simulated near-field reconstruction, rotated 3 × 3 aperture array

Figure 5.5: Simulated 3 × 3 aperture array with second-order correction

a realistic coded aperture, and a gamma-ray enters a general ‘pinhole’ (appendix figures A.10 and A.11, page 81).

Imaging geometry determines the maximum angle of incidence of a gamma-ray that enters a general ‘pinhole’ in the worst-case scenario. The highly simplistic mathematical analysis (section 5.1.1, page 23) can then be applied to both specific coded apertures and particular imaging geometries (appendix A.11, page 80).

For a tungsten coded aperture and the energy of Technetium-99m ($^{99\mathrm{m}}$Tc), for example, variation of imaging geometry, aperture thickness and ‘pinhole’ width, applied to appendix equations A.34 and A.38, generates a family of curves (figure 5.6). ΔI is the maximum change in detector intensities due to a point source S, which is at a height h above a square detector of length of side w. Note that the ratio h/w is used.

5.1.5 A limited field of view

The lowest envelope represents an ideal coded aperture (figure 5.6). For true pinholes, an increase in aperture thickness greatly increases attenuation, and the solid lines increase in minimum value. Imaging geometry has less of an effect with respect to the ideal curve.

For finite ‘pinholes’, an increase in the ratio of aperture thickness to ‘pinhole’ width again increases attenuation. The roll-off of the dashed curves shifts away from the ideal curve toward a far-field geometry. Nevertheless, the change in intensities can still be limited by means of the FOV.

5.1.6 Realistic aperture simulation

Relative to the simulation of ideal coded apertures, where the aperture ‘guides’ each gamma-ray that is traced, the physical properties of both the transparent and the opaque aperture elements are included. Attenuation ‘tubes’ can be designed to be, and are modelled as completely opaque.

For all points of the source, where each point radiates isotropically, at least one line is traced through all opaque and all transparent coded aperture elements. Multiple lines per element increase simulation accuracy. The point of intersection of each line with the plane of the detector is found. For a given line, the activity at

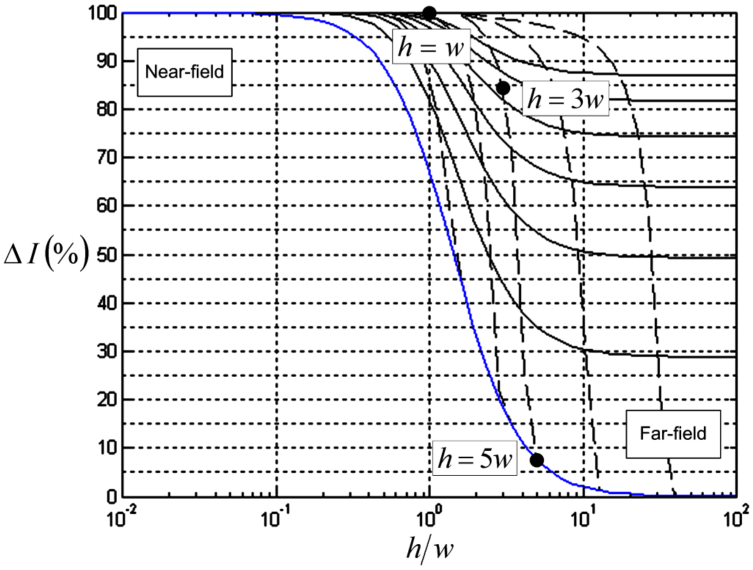

Figure 5.6: Plot of point source detector intensities for realistic apertures

the detector is calculated, based on the activity of and physical distance from the corresponding point source. The activity is also attenuated based on the distance of opaque aperture material traversed.

Note that second-order artifact correction is henceforth applied throughout, unless otherwise indicated. An aperture thickness to 'pinhole' width ratio of 3 corresponds to the central dashed curve (figure 5.6). A single realistic, as opposed to a single ideal coded aperture, leads to the presence of additional artifacts, which can only be the result of finite aperture properties (figure 5.7, relative to figure 4.6, page 20).

A 3×3 array of realistic limited-FOV coded apertures reduces near-field artifacts, but horizontal and vertical lines contribute a new 'tartan' artifact to the image (figure 5.8). A 5×5 array of coded apertures decreases the 'tartan', and the average contrast of a unique FOV can be shifted toward that of an adjacent FOV (figures 5.9 and 5.10).

Near-field artifacts are clearly reduced by the use of an array of coded apertures under both ideal and realistic aperture conditions. Relative to ideal coded apertures, the primary differences are structural: both the width of the 'pinholes' and the thickness of the aperture material must be finite. The next sections deal with each aspect in turn.

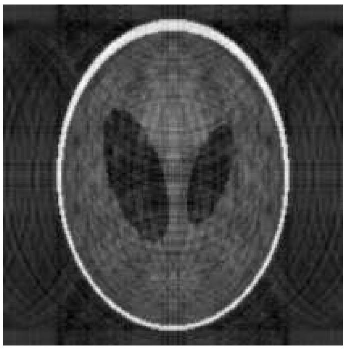

Figure 5.7: Simulated near-field reconstruction, realistic aperture

Figure 5.8: Simulated near-field reconstruction, realistic 3 × 3 aperture array

Figure 5.9: Simulated near-field reconstruction, realistic 5 × 5 aperture array

Figure 5.10: Simulated realistic 5 × 5 aperture array with contrast adjustment

5.2 Minimal ‘pinholes’

5.2.1 The partial volume effect

Use of finite ‘pinholes’ must introduce blur. The minimum ‘pinhole’ dimensions are, however, limited by the partial volume effect.

If a true pinhole projects a point source onto a single pixel of a perfect detector, the projection is represented correctly. If the projection is recorded by adjacent detector pixels, the activity is distributed between those pixels: the total activity remains unchanged but the measured peak is no longer correct [1].

This problem is known as the partial volume effect [1], and its solution requires the illumination of a 2 × 2 detector pixel area by means of a finite ‘pinhole’ area [2, 22]. One pixel is then always fully illuminated and the peak of the measured activity is correct. A theoretical projection β of 2×2 detector pixel area is centred at the point of intersection (appendix figure B.7, page 93).

5.2.2 Sampling considerations

A coded aperture pattern is a discrete binary array. Reconstruction operates on the sampled multiplexed data. Theoretically, a single point source reconstructs perfectly if the projected pattern is sampled as a single array of impulses or δ functions, all equal in amplitude and in the pattern of a single coded aperture cycle. Impulses due to an isotropic point source of radiation S are measured by specific pixels of the detector (figure 5.11).

Three parallel grids can be used to represent the discrete points of a planar source, the true pinholes of a coded aperture and the pixels of a detector. If these grids are aligned, a perfect detector would measure an impulse array for each point source.

If these grids are not aligned, the impulse arrays would undergo the partial volume effect. The replacement of true pinholes with transparent coded aperture elements, which illuminate a 1 × 1 detector pixel area, would increase blur but would make the system less susceptible to the partial volume effect.

Regardless of grid alignment, the partial volume effect is removed by the illumination of a 2×2 detector pixel area. The increased projection area would, however, result in

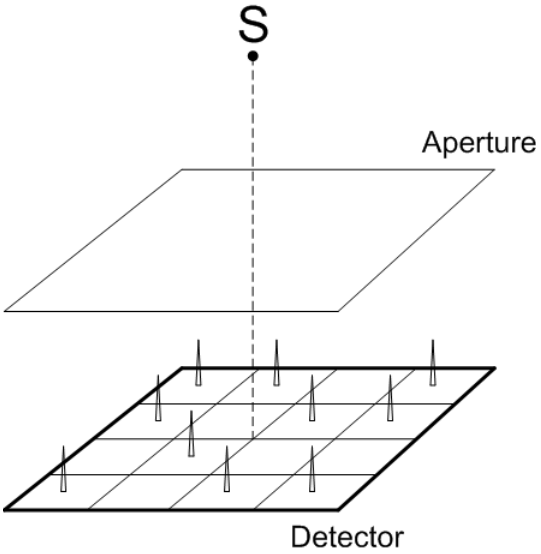

Figure 5.11: Schematic of a projected array of impulses

the measurement of adjacent impulse patterns and in the reconstruction of additional blur.

5.2.3 System limitations

Gamma camera pixel size limits image resolution, as it is the smallest interval at which samples can be obtained. Resolution is also limited by the requirements of the partial volume effect, and by the PSF of the detector.

The resolution of a coded aperture can be designed for optimal performance with a specific gamma camera [10], without modification of either the open fraction of the material or the FOV of the system. A decrease in the size of all pattern elements can be balanced by an increase in the total number of elements – achieved with the use of a larger prime.

The illumination of a 1×1 detector pixel area sets a sample threshold, below which a greater number of pattern elements cannot be measured. Any further enhancement of aperture resolution must reduce the open fraction of the aperture material. The coded aperture pattern projections are idealised and perfectly aligned (figures 5.12, 5.13 and 5.14). Note that dotted lines represent detector pixel boundaries.

Apart from the partial volume effect, a coded aperture element that illuminates a 1×1 detector pixel area is then optimal. A finite as opposed to a point source,

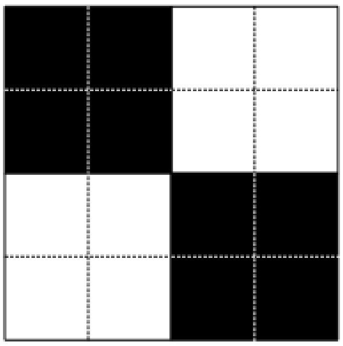

Figure 5.12: Schematic of a 2 × 2 detector pixel area projection

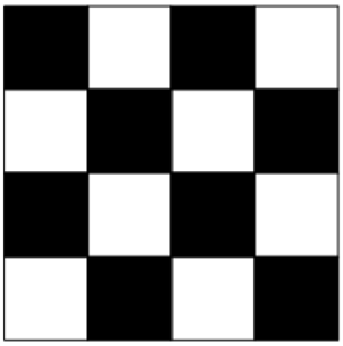

Figure 5.13: Schematic of a 1 × 1 detector pixel area projection

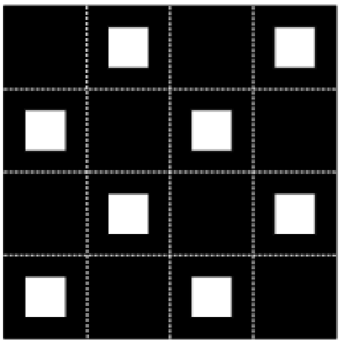

Figure 5.14: Schematic of a < 1 × 1 detector pixel area projection

however, must increase the illuminated area and must therefore reduce the severity of the partial volume effect.

5.2.4 Ideal finite ‘pinhole’ simulation

Relative to the simulation of ideal coded apertures, finite as opposed to true pinholes are used. An otherwise ideal aperture omits the artifacts that are introduced by aperture thickness or by transparency of the aperture material.

Two point sources positioned on the image diagonal, with the source and system grids perfectly aligned, give a sharper reconstruction with a 1×1 as opposed to a 2×2 detector pixel area projection (figures 5.15(a) and 5.15(b)). The peak intensities are measured correctly in both cases.

The worst-case partial volume effect is obtained if the upper source is shifted by half a pixel along both axes. The 1×1 detector pixel area projection is clearly affected (figures 5.15(c) and 5.15(d)).

A grid that represents the source as discrete points is useful for computational purposes; but multiple grids of varied shifts are then necessary to approach continuity. Finite sources are modelled by the addition of a second point source grid, shifted one quarter of a pixel along both axes relative to the first grid. The upper source remains misaligned, but the partial volume effect becomes less severe for the 1×1 detector pixel area projection (figures 5.15(e) and 5.15(f)).

The distributed Shepp-Logan phantom is represented as a grid of point sources, all shifted by half a pixel along both axes for worst-case alignment. Resolution of the 1×1 detector pixel area projection is superior to that of the 2×2 detector pixel area projection (figures 5.16 and 5.17).

As opposed to a perfect gamma camera PSF, increased blur is applied to the multiplexed data by means of a Gaussian PSF with standard deviation $\sigma = 1.27$ (appendix A.12, page 83). The reconstructions show a close link between the ability to enhance resolution, or lack thereof, and the PSF of the gamma camera (figures 5.18 and 5.19).

A 2×2 detector pixel area projection is still used [2, 22], although earlier work has stated that such a ‘conservative’ approach is not necessary [10]. It is clear that the partial volume effect has less influence on finite sources and no significant influence

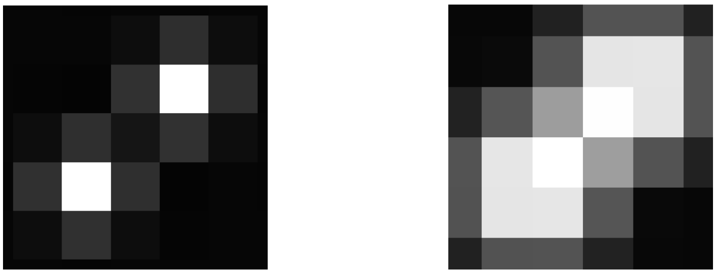

(a) 1 × 1 aligned

(b) 2 × 2 aligned

(c) 1 × 1 misaligned

(d) 2 × 2 misaligned

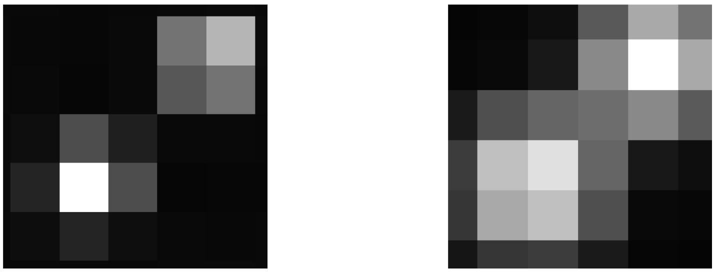

(e) 1 × 1 finite

(f) 2 × 2 finite

Figure 5.15: Simulated reconstructions of point and finite point sources

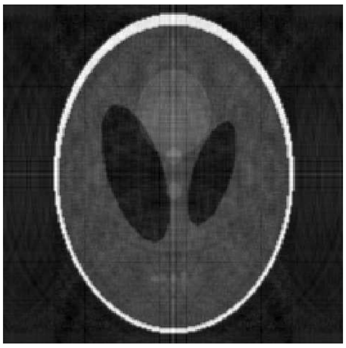

Figure 5.16: Simulated near-field reconstruction, 1 × 1 area, perfect PSF

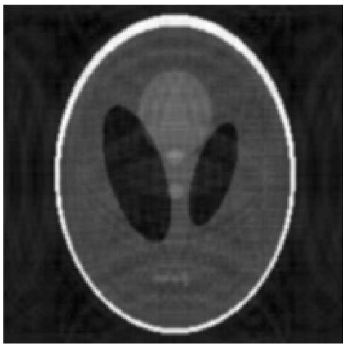

Figure 5.17: Simulated near-field reconstruction, 2 × 2 area, perfect PSF

Figure 5.18: Simulated near-field reconstruction, 1 × 1 area, $\sigma = 1.27$ PSF

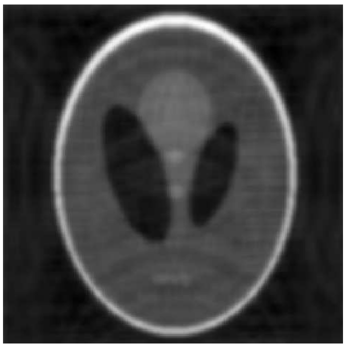

Figure 5.19: Simulated near-field reconstruction, 2 × 2 area, $\sigma = 1.27$ PSF

on distributed sources. While the use of a 1 × 1 detector pixel area projection is non-conventional, it does have the potential to enhance resolution.

5.3 Highly transparent material

5.3.1 Aperture thickness

Collimator septa are of a sufficient thickness to attenuate gamma-rays that impact beyond a given angle of incidence [1]. If the septa are highly transparent to gamma-rays, adjacent detector regions are illuminated and the septa cease to perform collimation. A highly transparent collimator is illuminated by an isotropic point source of radiation S (figure 5.20).

With respect to coded apertures, thickness of the aperture material introduces collimation effects [2, 10, 22]. The convolution model does not hold and thickness artifacts result.

A coded aperture can, for example, be designed to match a 10× enhancement in the spatial resolution of a gamma camera (section 5.2.3, page 32). However, aperture thickness must limit the minimum 'pinhole' width if collimation effects are to be avoided [16]. Aperture thickness also constrains the techniques that are available for coded aperture manufacture.

Thin coded apertures are desirable but become highly transparent (appendix A.13, page 83). Although coded apertures with thicknesses in the micrometer range do exist [33, 39, 40, 43], use is limited to photon energies at which the material thickness remains opaque. A conventional coded aperture typically has an attenuation above 90 %, preferably in the order of 99 % [2, 22, 43].

5.3.2 High transparency

A relatively thin and therefore highly transparent aperture material attenuates a low percentage of incident gamma-rays, and decreases the contrast of, and the ability to discern features within the recorded image (appendix figure C.12, page 98). Correlation allows the contrast of the reconstructed image to be maintained.

A pixel of the detector can record a limited number of counts of radioactivity, or

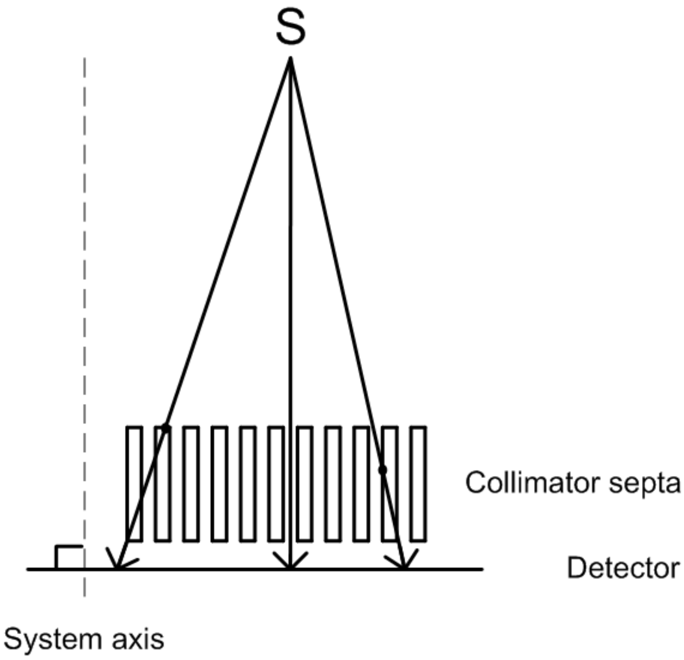

Figure 5.20: Schematic of a highly transparent parallel-hole collimator

has a limited bit-depth [1]. A decrease in contrast then increases quantization of the measured data. For example, a decrease in the vertical resolution of a signal reduces signal quality (appendix figures B.8 and B.9, page 94). Correlation searches for the expected aperture pattern, but the quantized pattern is less recognizable [2] and noise results.

If a pixel of the gamma camera has a sufficient bit-depth, and if a suitable number of counts of radioactivity are obtained, high transparency of the coded aperture need not lead to significant quantization effects: the SNR need not be reduced. This hypothesis is applicable regardless of the choice of aperture material or photon energy. For example, at the energy of ^{99m}Tc, a 1 mm thick tungsten aperture is opaque with an attenuation of 97 %. By contrast, at the same energy, 100 μm of tungsten is highly transparent with an attenuation of 29 %. Higher energy isotopes require thicker aperture material.

A thin aperture could be used to reduce collimation effects but count statistics would limit practicality [2, 22]. Specifically, at an energy higher than that for which the coded aperture was designed, the image acquisition time would have to be increased [22]. Coded apertures continue to be designed so that closed pattern elements remain opaque [2, 33, 39, 43]. The 'bazooka' gamma-ray microscope has an interesting modification: aperture material is opaque at the energy of interest, while at higher energies both the aperture and the scintillator become transparent [40].

A thin and highly transparent aperture material may be a simplistic tactic with respect to the reduction of thickness artifacts. It may further be considered obvious that the associated decrease in the SNR can be offset by an increase in the number of counts of radioactivity [22]. Nevertheless, deliberately high-transparency coded apertures as proposed in this thesis are not intuitive: a coded aperture continues to function under conditions in which a collimator is rendered functionless.

5.3.3 Transparency simulation

The digitization effects of the gamma camera are included relative to the simulation of realistic coded apertures. The multiplexed data is scaled by a constant prior to reconstruction, so that the maximum pixel intensity corresponds to a defined gamma camera bit-depth. Non-integer values are then rounded so as to quantize the data.

An 8-bit gamma camera and a 97 % attenuation aperture would have little effect on the contrast of the multiplexed data. Collimation effects lead to thickness artifacts (figure 5.21).

An otherwise identical but highly transparent aperture, with an attenuation of 29 %, would be expected to reduce thickness artifacts. Low contrast of the multiplexed data results in significant noise (figure 5.22).

A 16-bit gamma camera and 97 % attenuation aperture improve image quality (figure 5.23, relative to figure 5.21). The additional gamma camera bit-depth is also sufficient for the highly transparent aperture pattern to remain recognizable. The image is unaffected by noise and thickness artifacts are reduced (figure 5.24, relative to figure 5.21).

An aperture that is 10× thinner, for example, simplifies manufacture or allows for a 10× improvement in the resolution of the aperture without an increase in collimation effects. The gamma camera count rate becomes the limiting factor. There are indications that the gamma camera count rate may be able to follow suit [40, 44].

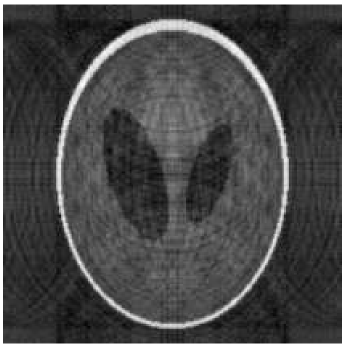

Figure 5.21: Simulated near-field reconstruction, 8-bit opaque

Figure 5.22: Simulated near-field reconstruction, 8-bit highly transparent

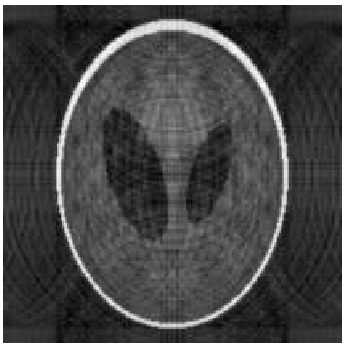

Figure 5.23: Simulated near-field reconstruction, 16-bit opaque

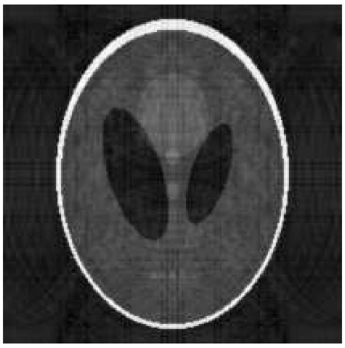

Figure 5.24: Simulated near-field reconstruction, 16-bit highly transparent

5.3.4 Transparency simulation with count statistics

The count statistics that are associated with radioactivity are an important aspect that must be modelled. Relative to the transparency simulation, the value of each pixel is altered in accordance with the Poisson distribution [22] (appendix A.14, page 84). The projected aperture pattern becomes less recognizable, and is expected to add further noise to the reconstruction.

A line set at 45 ° to the horizontal is used as a digital phantom (figure 5.25), so as to allow for comparison with experimental results (section 6.2.3, page 52). Count statistics require an increased bit-depth if the SNR is not to be adversely affected. The reconstructions for a 29 % attenuation aperture improve with the number of counts acquired (figures 5.26, 5.27 and 5.28). Note that the number of counts refers to the maximum single pixel count within the multiplexed data.

The reconstructions show that despite the presence of count statistics, the concept of high-transparency coded apertures does remain applicable. The sensitivity of the gamma camera is not modelled, but affects acquisition time and thus clinical practicality, all of which are discussed in due course.

5.4 A matter of efficiency

5.4.1 Count statistics

As opposed to a single coded aperture, an array of limited-FOV coded apertures can reduce near-field artifacts. The FOV of the system remains unaltered, but that of each individual coded aperture decreases, as does the number of counts of radioactivity that are acquired.

A coded aperture that illuminates a 1×1, as opposed to a 2×2 detector pixel area can give a resolution that is optimal without a change in the open fraction of the aperture material. A smaller pattern element collects fewer counts of radioactivity.

Thin and highly transparent coded aperture material simplifies aperture construction and can reduce thickness artifacts. A greater number of counts of radioactivity must be acquired if the SNR is to be maintained.

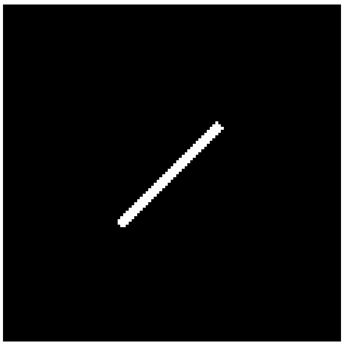

Figure 5.25: 2D digital line phantom

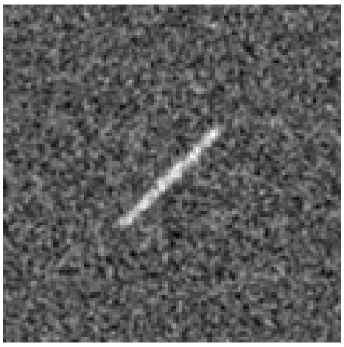

Figure 5.26: Simulated line source reconstruction, 256 counts

Figure 5.27: Simulated line source reconstruction, 8192 counts

Figure 5.28: Simulated line source reconstruction, 65536 counts

5.4.2 Ultra-near-field conditions

The activity that is collected by a single collimator hole increases as the source nears the detector, but fewer holes are illuminated [1]. That is, resolution increases but efficiency does not alter. By contrast, for a coded aperture at a fixed imaging ratio, efficiency increases as the source nears the detector but resolution does not alter.

An ultra-near-field coded aperture design can allow for an increase in system sensitivity and thus count statistics, provided that the sensitivity of the gamma camera is able to follow suit. (Further detail relating to the measurement of system sensitivity is provided in section 6.2.3, page 52.) The novel theoretical concepts could then be implemented without a decrease in count statistics, and without change in either dose or acquisition time (appendix A.15, page 84).

Severe artifacts are expected to arise under ultra-near-field conditions. An array of thin and highly transparent limited-FOV coded apertures, however, has the potential to control both near-field and thickness artifacts, while the use of a 1×1 detector pixel area projection can achieve a resolution that is optimal.

5.4.3 Ultra-near-field simulation

Relative to the simulation of realistic coded apertures, both the digitization effects of the gamma camera and count statistics are included. The only alteration is the use of an ultra-near-field geometry.

Acquisition bit-depth is altered for each specific system (appendix equations A.42 and A.43, page 84), so that both dose and acquisition time remain constant. The radiation attenuation ‘tubes’ are modelled so as to result in the absence of data in the regions that correspond to finite ‘tube’ walls.

There are $16\times$ the number of counts at $1/4$ the distance, but the reconstruction for a single realistic aperture suffers from significant artifacts. An ultra-near-field implementation of the novel theoretical concepts, however, leads to both artifact reduction and an enhancement of resolution.

A single prior-state-of-the-art opaque self-supporting coded aperture, with a 2×2 detector pixel area projection, is reconstructed (figure 5.29). Note that all changes in bit-depth are quoted relative to this figure. For example, bit-depth increases by 4 under ultra-near-field conditions (figure 5.30). A novel 3×3 array of highly transparent non-self-supporting coded apertures, with a 1×1 detector pixel area projection, is reconstructed (figure 5.31). The bit-depth decreases by 0.5, but increases by 3.5 under ultra-near-field conditions (figure 5.32). Note that the results are presented without interpolation in the regions that correspond to 'tube' walls, and as such, the RMSE measurements (appendix table E.2, page 105) do not consider the absent data.

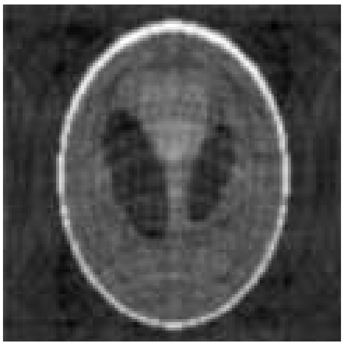

Figure 5.29: Simulated near-field reconstruction, self-supporting opaque

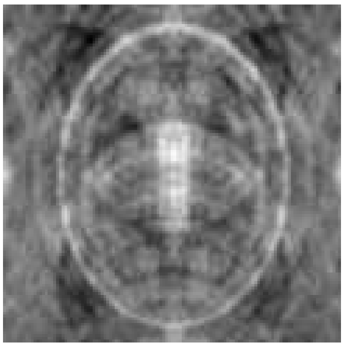

Figure 5.30: Simulated ultra-near-field reconstruction, self-supporting opaque

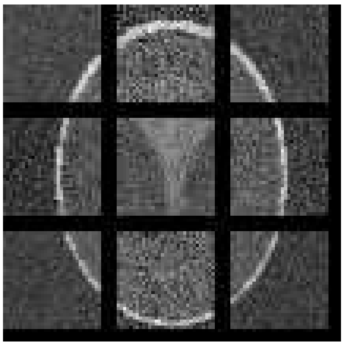

Figure 5.31: Simulated near-field reconstruction, highly transparent array

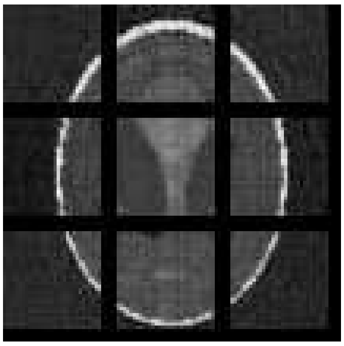

Figure 5.32: Simulated ultra-near-field reconstruction, highly transparent array

Chapter 6

Experimentation

6.1 Apparatus

6.1.1 Gamma camera frame

A specialised aluminium frame allows coded apertures to be mounted onto a Philips Axis — dual head variable angle gamma camera. The attachment mechanism is identical to that of the existing exchangeable collimators. The four original Philips rings for use with the camera latching mechanism are visible (appendix figure D.1, page 99). Note the solid sheet for additional protection of the camera crystal.

A circular bearing in the base of the frame is fitted with a plate that allows for rotation. The plate is able to rotate freely within the plane of the frame, but can be accurately secured at a rotation of 90 °. Photographs of the circular bearing, plate and fitted plate are presented (appendix figures D.2, D.3 and D.4).

An aperture carriage is bolted onto the plate and contains a tripod mechanism, the upper surface of which can be aligned so that it is parallel to the camera crystal. The tripod mechanism (appendix figure D.5) is bolted onto the rotation stage (appendix figure D.6).

A coded aperture is enclosed by a square lead radiation attenuation 'tube' to form a single fixed unit. The lower half of a lead 'tube' has been machined to fit a coded aperture (appendix figures D.7 and D.8). The upper surface of the tripod mechanism supports this unit, and forms a plane that allows for alignment on both the x and the y axes. The unit extends above the mechanism toward the source, and below the mechanism toward the base of the aluminium frame (appendix figure D.9).

This arrangement allows for the coded aperture to be rotated by 90 °, and to be aligned so that it is both centred with respect to the axis of rotation and is parallel to the camera crystal. Use of a specific carriage and coded aperture pair is, after initial alignment, then repeatable (appendix A.16, page 85).

Note that the design of the gamma camera frame could allow an array of coded apertures, carried on a single sheet of material, to be enclosed by a composite lead 'tube', which could contain one 'tube' for each aperture of the array. The single fixed unit could then be rotated and aligned in precisely the same manner as that for a single coded aperture.

6.1.2 Coded aperture design

A prior-state-of-the-art coded aperture [2, 22] is constructed so as to provide a point of reference. This allows for a direct comparison of LEHR parallel-hole collimator imaging, and of both prior-state-of-the-art and novel coded aperture reconstructions.

The ideal aperture pattern requires square holes with vertical walls, if the autocorrelation function of the sampled projection is to be optimal. Round holes reduce efficiency and do not meet this criterion.

The circular bearing is inscribed within the border of the aluminium frame. The square radiation attenuation 'tube' of the square aperture extends toward the base of the frame, and must be inscribed within the circular bearing. This sets the maximum FOV of the coded aperture. Note that expense aside, a gamma camera frame and coded aperture could be designed to utilise the full FOV of the camera crystal.

An anti-symmetric pattern from the NTHT MURA family of coded apertures is used [2, 11, 14, 15]. The pattern has an open fraction of 12.5 %, is self-supporting and allows for near-field artifact reduction by means of a 90 ° rotation of the aperture [19].

The partial volume effect requires the illumination of a 2 × 2 detector pixel area [2, 22]. 1.2 mm × 1.2 mm square holes are then required at a 1:1 imaging ratio (appendix A.17, page 86). A single 61 × 61 element mosaic then achieves both the correct aperture properties and the maximum FOV at 145.2 mm × 145.2 mm.

6.1.3 Laser fabrication

Technical and practical challenges are associated with aperture construction. Materials with high attenuation characteristics include uranium, platinum, gold, tungsten and lead [1, 2]. Uranium cannot be tooled without license, platinum and gold are costly, tungsten has an exceedingly high melting point and is both hard and brittle, and lead is soft and is subject to creep.

A 1 mm thick tungsten sheet has an attenuation of 97 % at the energy of $^{99\mathrm{m}}$Tc. With respect to aperture construction techniques such as etching or deposition, a thickness of 1 mm is impractical unless laminations are used [19].

Laser drilled holes provide practical fabrication at the lowest cost. The 1860 identical holes are cut in a single 1 mm tungsten sheet (appendix figure D.10, page 102), in a random as opposed to a linear pattern to reduce heat effects. A prior-state-of-the-art tungsten coded aperture with an attenuation of 97 % results (figure 6.1).

6.1.4 Novel coded aperture

An array of limited-FOV coded apertures has the potential to reduce near-field artifacts, but would give better count statistics with MURA as opposed to self-supporting NTHT MURA patterns. A 1 × 1 as opposed to a 2 × 2 detector pixel area projection has the potential to enhance resolution, but would depend on the PSF of the gamma camera.

Of the novel theoretical concepts, high transparency can facilitate aperture construction. That is, thin apertures do have the potential to simplify the fabrication of patterns that are not self-supporting; and, if practical, can be used in the construction of non-self-supporting limited-FOV coded aperture arrays.

6.1.5 Laser ablation

100 μm thick tungsten foil has an attenuation of 29 % at the energy of $^{99\mathrm{m}}$Tc. The highly transparent coded aperture pattern is otherwise identical to that of the prior state of the art. The tungsten foil is first bonded to an aluminium plate, so as to hold the offcuts in position. The border of each of the 1860 identical holes is then

laser ablated, in a random as opposed to a linear pattern to reduce ablation heat effects.

After ablation the aluminium plate and the offcuts are separated from the tungsten foil, and a new aluminium plate is bonded to the tungsten so as to provide mechanical strength. A highly transparent tungsten coded aperture with an attenuation of 29 % results (figure 6.2).

6.2 Results

6.2.1 Protocol

An ultra-near-field geometry does have the potential to increase system sensitivity, but such an increase is highly dependent on the sensitivity of the gamma camera. A near-field geometry is used throughout.

The dual heads of the gamma camera are positioned with one camera below, and the second above the phantom. A coded aperture is mounted on the lower camera, and the LEHR parallel-hole collimator is mounted on the upper camera (figures 6.3 and 6.4). Acquisition is carried out with both cameras simultaneously. The coded aperture is then rotated by 90 ° in the plane that is parallel to the camera crystal, and acquisition is repeated.

A rotation of the aperture would not be necessary if the dual camera heads were fitted with the mask and the anti-mask respectively [31]. The total acquisition time would then halve, but second-order artifact reduction would only be accurate if identical imaging geometries were used. The mask and the anti-mask imaging geometries would differ for all planes other than the central plane of a 3D source.

Note that in the sections that follow, coded aperture image acquisition times include the mask image and the anti-mask image. Neither zero-order nor first-order artifact reduction [18] is applied. The mask anti-mask technique [18, 20] and correlation decoding [5] are used throughout.

Collimator and coded aperture images are acquired at identical near-field geometries, with the source positioned at a distance of 20 cm from the appropriate camera crystal unless otherwise stated. Note that the resolution of the LEHR collimator image would be expected to improve as the source approaches the crystal [1].

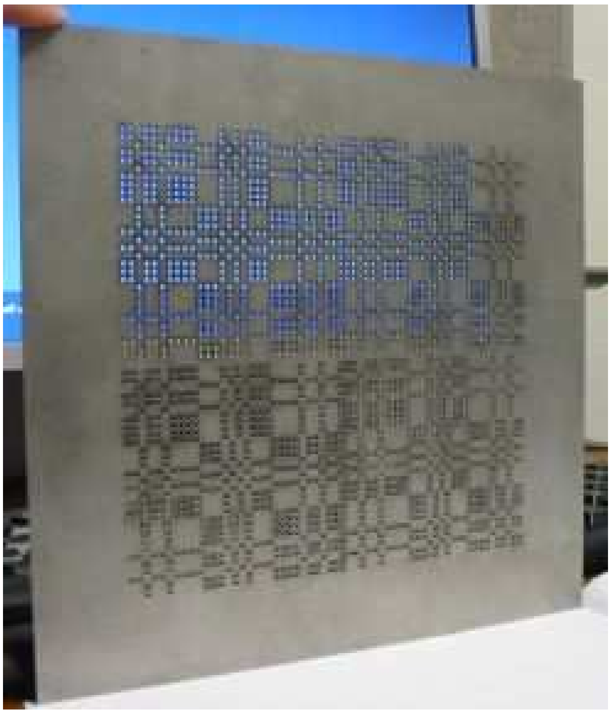

Figure 6.1: Prior-state-of-the-art 97 % attenuation tungsten coded aperture

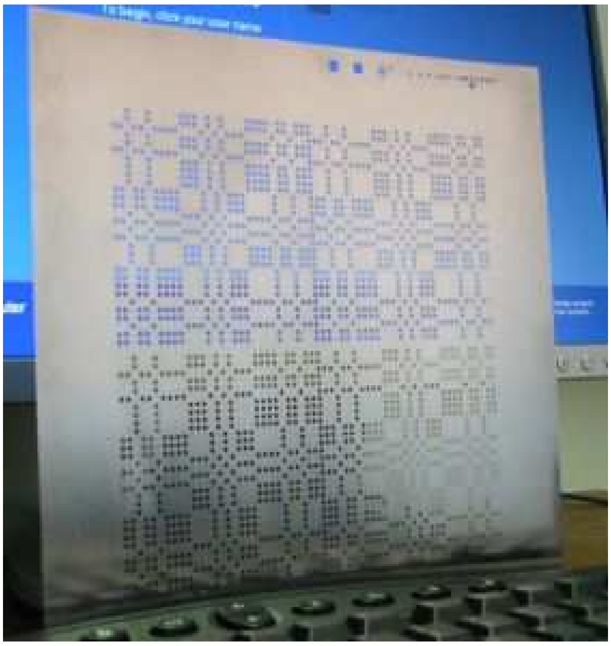

Figure 6.2: Novel 29 % attenuation tungsten coded aperture

Figure 6.3: Gamma camera frame mounted on the Philips Axis

Figure 6.4: Dual gamma camera heads with collimator and coded aperture

6.2.2 Point and line sources

A single drop of $^{99\mathrm{m}}$Tc provides a point source. Resolution of the prior-state-of-the-art coded aperture is superior to that of the collimator (figures 6.5 and 6.6), but the cross-artifact is clearly visible in the coded aperture image (figure 6.6). The SNR decreases for the high-transparency aperture (figures 6.7 and 6.8).

A capillary tube dipped in $^{99\mathrm{m}}$Tc fills by capillary action. Line source count statistics are poor for the 1 minute prior-state-of-the-art acquisition (figures 6.9, 6.10, 6.11 and 6.12). Near-field artifacts manifest in the form of ghosting.

6.2.3 Syringe source

A $^{99\mathrm{m}}$Tc 1 ml syringe source is positioned at a distance of 20 cm from the camera crystal. Source activity is altered to allow for the measurement of system sensitivity [45], for the Philips Axis and the 29 % attenuation tungsten coded aperture by way of example (appendix table E.3, page 106).

Based on count rate data, a 24.4 MBq (660 μCi) syringe source is prepared, which corresponds to a count rate of 123000 counts per second (cps). For the prior state-of-the-art acquisition, noise is reduced at a maximum pixel count of 3270 as opposed to 286. Acquisition times are 15 minutes, 90 seconds and 20 minutes (figures 6.13, 6.14 and 6.15, respectively). Note that the number of counts refers to the maximum single pixel count within the multiplexed data. Superior coded aperture resolution is particularly evident where the syringe tapers at upper right, but near-field artifacts remain.

For the high-transparency aperture, count statistics are poor at a maximum pixel count of 285, but are significantly better at a maximum pixel count of 8248. Acquisition times are 1 minute and 30 minutes (figures 6.16 and 6.17, respectively). The quality of the highly transparent aperture image begins to approach that of the opaque aperture image. The results are comparable to those predicted by the simulations (figures 5.26 and 5.27, page 42), and certainly do verify the concept of highly transparent coded apertures. This is believed to be the first time that an intentionally highly transparent coded aperture has been designed, fabricated and used to acquire experimental images.

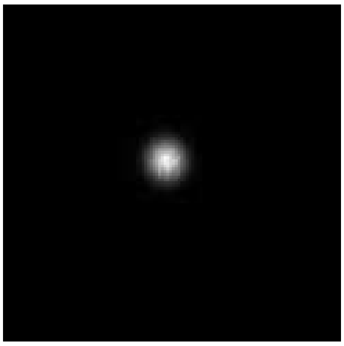

Figure 6.5: Acquired point source, LEHR collimator

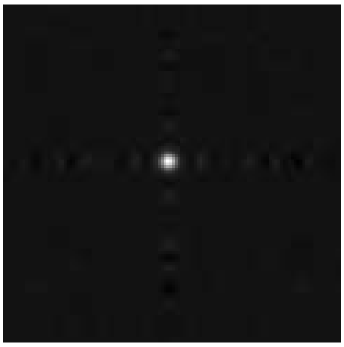

Figure 6.6: Acquired point source, opaque aperture

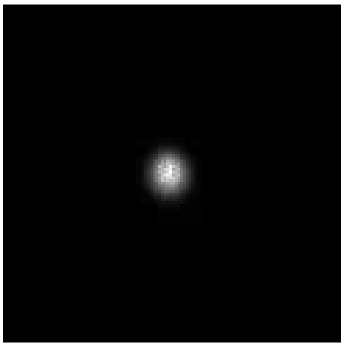

Figure 6.7: Second acquired point source, LEHR collimator

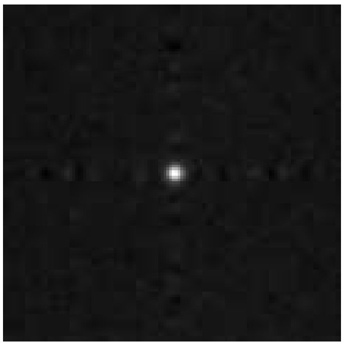

Figure 6.8: Second acquired point source, highly transparent aperture

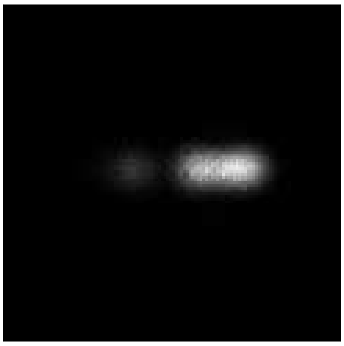

Figure 6.9: Acquired line source, LEHR collimator

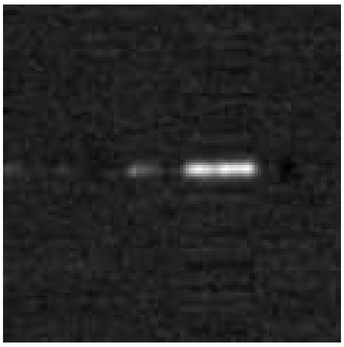

Figure 6.10: Acquired line source, opaque aperture, 1 minute

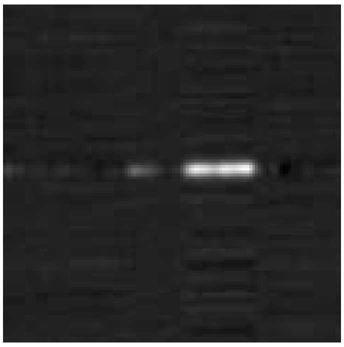

Figure 6.11: Acquired line source, opaque aperture, 12 minutes

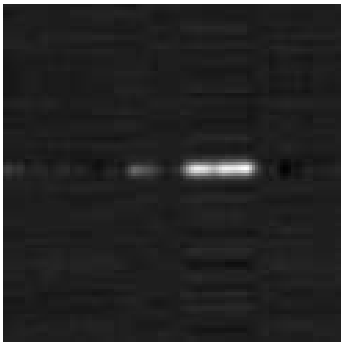

Figure 6.12: Acquired line source, opaque aperture, 20 minutes

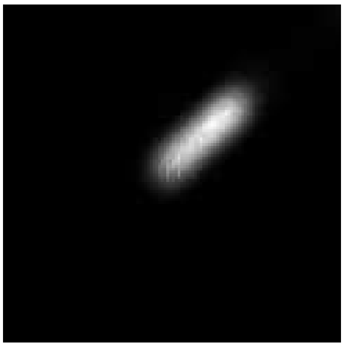

Figure 6.13: Acquired syringe source, LEHR collimator

Figure 6.14: Acquired syringe source, opaque aperture, 286 counts

Figure 6.15: Acquired syringe source, opaque aperture, 3270 counts

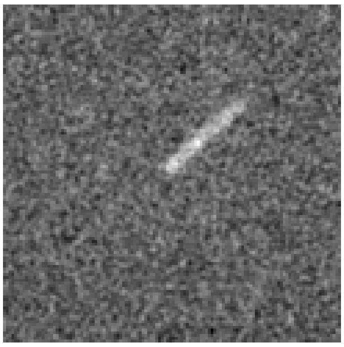

Figure 6.16: Acquired syringe source, highly transparent aperture, 285 counts

Figure 6.17: Acquired syringe source, highly transparent aperture, 8248 counts

If not limited by the gamma camera, a source in the region of 244 MBq (6.6 mCi) could, for example, allow for 24 minute acquisitions of 16-bit highly transparent aperture images. This may not be clinically realizable.

6.2.4 Printed phantoms

Ink is mixed with $^{99\mathrm{m}}$Tc and is injected into a printer cartridge [46]. Repeatable 2D phantoms of distributed sources can then be printed in radioactive ink, where the ink and $^{99\mathrm{m}}$Tc volumes, together with digital phantom pixel intensities, allow for the calculation of printed phantom activity [46, 47]. LEHR collimator images are acquired with the source positioned at both 20 cm and 10 cm from the camera crystal. All collimator and coded aperture acquisition times are 15 minutes and 30 minutes, respectively.

A printed Shepp-Logan phantom provides a distributed source (appendix figure D.11, page 103). The prior-state-of-the-art acquisition suffers from severe noise (figures 6.18, 6.19, and 6.20). Neither near-field nor thickness artifacts are visible, and noise negates the enhanced resolution advantage.

A printed bar phantom provides a second distributed source (appendix figure D.12). The LEHR collimator begins to resolve the 5 mm quadrant at lower left, which has 1 cycle per cm (figures 6.21 and 6.22). The prior-state-of-the-art acquisition again reconstructs with severe noise (figure 6.23).

Simple multiplication of the 10 cm collimator image and the coded aperture image decreases noise outside of the object relative to the aperture image, while the resolution advantage over the collimator image appears to be retained (figures 6.24 and 6.25). This qualitative improvement is particularly evident in the 5 mm bar phantom quadrant at lower left.

Note that the collimator image provides an indication as to which regions of the source actually exist. Multiplication serves as a basic strategy, but is likely to increase noise within the object.

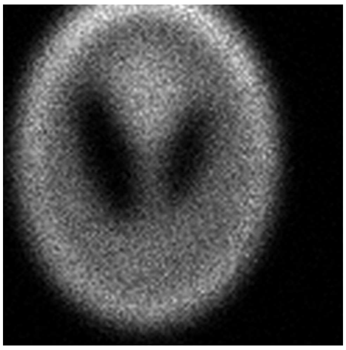

Figure 6.18: Acquired Shepp-Logan phantom, LEHR collimator, 20 cm

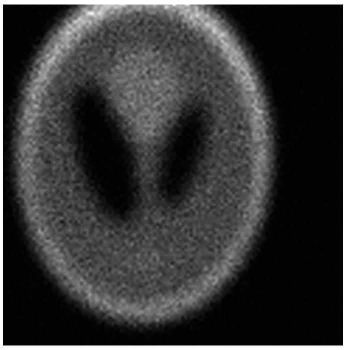

Figure 6.19: Acquired Shepp-Logan phantom, LEHR collimator, 10 cm

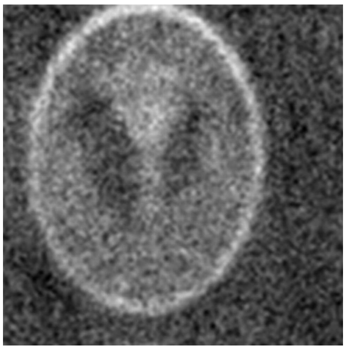

Figure 6.20: Acquired Shepp-Logan phantom, opaque aperture

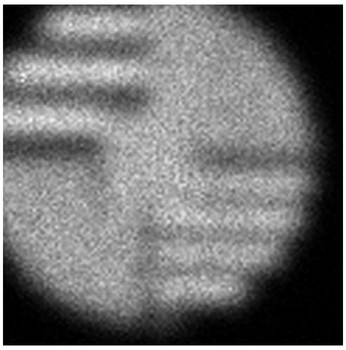

Figure 6.21: Acquired bar phantom, LEHR collimator, 20 cm

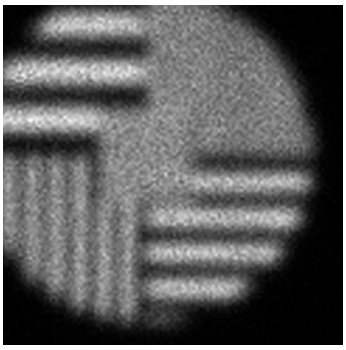

Figure 6.22: Acquired bar phantom, LEHR collimator, 10 cm

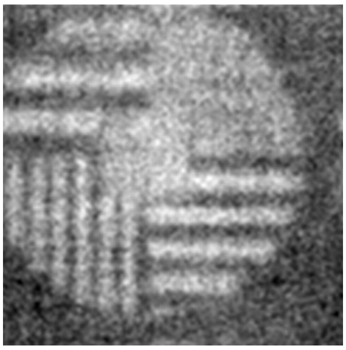

Figure 6.23: Acquired bar phantom, opaque aperture

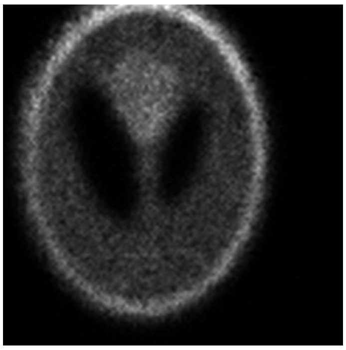

Figure 6.24: Acquired Shepp-Logan phantom, combined data

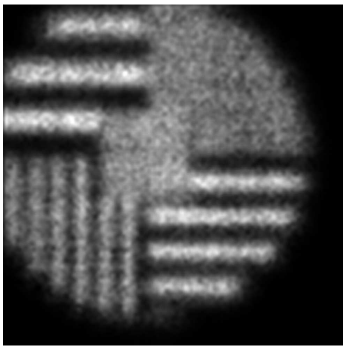

Figure 6.25: Acquired bar phantom, combined data

Chapter 7

Conclusion

7.1 Summary

7.1.1 Simulation

The use of coded apertures under near-field conditions can be problematic [10]. Prior work has significantly advanced the field, particularly in terms of the mask anti-mask technique [18, 20], but has clearly underscored the difficulties that are associated with distributed sources [5, 16, 19].

In this thesis, basic coded aperture theory is discussed, and is extended toward the simulation of highly idealised near-field conditions. While such simulations are of limited practical use, the line of reasoning makes it clear that near-field artifacts will be present even under the most perfect of aperture and imaging conditions.

An array of coded apertures, that is multiple coded apertures placed side-by-side in the form of a matrix, does have the potential to reduce near-field artifacts under both idealised and realistic coded aperture conditions. This novel technique not only reduces artifacts by means of geometry prior to reconstruction, but also allows for implementation of the mask anti-mask technique. An array of coded apertures creates a new perspective: prior SNR calculations and the existing artifact theory are no longer directly applicable.

Further idealised simulation in this study served to challenge the partial volume effect, which is one of the factors that typically limits coded aperture resolution. The practicality of an enhanced aperture resolution is, however, logically dependent on the PSF of the particular gamma camera.

A near-field imaging geometry worsens the collimation effects that are caused by thickness of the aperture material [2, 10]. Idealised simulation in this study again challenged the status quo, in this case with thin and deliberately highly transparent aperture material – a situation that is counter-intuitive and that differs significantly from that of collimators.

There is, of course, a trade-off: any one of these potential improvements comes at the cost of count statistics. Later simulation features therefore included the thickness, attenuation and 'pinhole' widths of realistic coded apertures, together with gamma camera digitization effects and the count statistics that are associated with radioactivity.

An ultra-near-field geometry, which for a standard coded aperture would significantly worsen artifacts, can theoretically allow all three potential improvements to be implemented without a reduction in count statistics, and without alteration of either dose or acquisition time.

Note that the suggested techniques should not be implemented without careful consideration of the specific gamma camera parameters. For example, if system sensitivity is relatively low, an array of coded apertures may prove more useful than a higher resolution coded aperture would do. It may similarly be preferable to remove near-field as opposed to only thickness artifacts.

7.1.2 Acquisition

System sensitivity was experimentally measured for the Philips Axis gamma camera and highly transparent coded aperture. The optimal count rate was achieved at relatively low source activities. Phantom-based experimental acquisitions served to verify both the simulator and the theoretical concept of high-transparency coded apertures.

Use of the prior state of the art in coded aperture technology and an existing gamma camera, together with straightforward artifact correction and simple reconstruction techniques, can give coded aperture images of non-distributed sources that are at least qualitatively comparable to high-resolution collimator images. Unlike collimators, the resolution of coded aperture systems can be enhanced.

With respect to the LEHR parallel-hole collimator, coded aperture acquisitions of non-distributed sources can be obtained in a fraction of the time. The resolution advantage is clearly visible, as are near-field artifacts.

Coded aperture reconstructions of distributed sources, however, suffer from severe noise despite lengthy acquisition times. As the source contains many more points of activity, fewer counts are available per point of reconstruction [11], and the anticipated near-field artifacts are concealed by poor count statistics. If the result is to be competitive, the complete acquisition time must be less than or equal to that of the collimator.

Simple multiplication appears to retain the qualitative coded aperture resolution advantage, but more sophisticated techniques are likely to give better results. An iterative MLEM reconstruction could, for example, accurately model both the geometry and the physics of the system [26, 27, 34].

7.2 Discussion

The coded aperture technique clearly requires significant improvement if the images are to be acceptable in a clinical setting. However, gamma cameras have been designed for use with collimators, and the count rate is not suited to the high efficiency of coded apertures. While a higher gamma camera count rate would be of little use for an LEHR collimator, it would be most useful for coded apertures.

That is, an increase in gamma camera sensitivity would allow for an improved collimator count rate, but the resolution would ultimately be limited by the width of the collimator septa. By contrast, coded aperture resolution can be enhanced if gamma camera sensitivity is improved.

If the gamma camera count rate were to allow for the acquisition of a relatively noise-free coded aperture image of a distributed source; in a practical time-frame, the collimator image could then be neglected. Artifacts would become visible if count statistics were to improve, but artifact-reduction techniques could be applied.

Based on the acquisitions of non-distributed sources, rapid imaging times can be achieved. Artifact-reduction techniques coupled with a sufficient gamma camera count rate may allow the same to be said of distributed sources. That is, coded apertures may have the potential to acquire high-resolution artifact-free images, and relative to collimator-based imaging, to acquire those images in a fraction of the time.

7.3 Recommendations

In this thesis, several concepts have been suggested, the core components of which have been presented at international conferences and published as patents (appendix F, page 107). As only high-transparency coded apertures have been studied under experimental conditions, there is much potential for further experimentation.

The possibility of tomography has not been excluded, but applicability of the concepts to 3D sources will differ to the 2D work of this thesis. Further investigation is certainly required.

The clinical practicality of a coded aperture is closely related to the pixel size, PSF and count rate of the gamma camera. Gamma camera specifications are therefore key to successful coded aperture implementation. If a high-count-rate gamma camera were designed for optimal coded aperture performance, it could theoretically allow distributed source imaging times to become competitive. Further investigation should therefore certainly be encouraged, with respect not only to coded aperture design, but also to radiation detector development.

Note that new high-count-rate detectors are being investigated. Recent developments include modular detectors [44], in which the multiple camera modules are mechanically, optically and electronically independent; so that a significant increase in count rate can be achieved.

Only once the image has been acquired in the best possible way does it make sense for software-based correction techniques to be applied. For example, as opposed to correlation decoding, an MLEM algorithm could be used to reconstruct the multiplexed data [26, 34].

The algorithm could use collimator data for the initial approximation, and may negate the need for mask and anti-mask acquisitions [27, 34]. The algorithm could also model the transparency of the aperture material and the count statistics that are associated with radioactivity [42] – an approach that may be ideally suited to the reconstruction of high-transparency coded aperture images.

In short, numerous possibilities do exist and, despite the difficulties, coded apertures may yet offer tremendous potential.

Appendix A

Mathematics

A.1 Basic acquisition

Coded aperture acquisition is modelled by:

$$R = O \ast A \tag{A.1}$$

where

$R =$ the recorded image
$O =$ the object
$A =$ the aperture
$\ast =$ convolution

Image reconstruction is then given by:

$$O' = R \otimes G \tag{A.2}$$

where

$O' =$ the reconstructed image
$G =$ the decoding array
$\otimes =$ correlation with periodic conditions

where the periodicity is associated with the nature of the aperture pattern [2, 5].

From equation A.1:

$$\begin{aligned} O' &= (O \ast A) \otimes G \\ &= O \ast (A \otimes G) \end{aligned} \tag{A.3}$$

The recorded image must be correlated with the same coded aperture pattern, in other words $A = G$ [2]. It is also a requirement that, in the ideal case, the autocorrelation function of the aperture pattern must be an impulse or δ function [5, 12]:

$$A \otimes G = \delta \tag{A.4}$$

Equation A.3 then gives an ideal reconstruction:

$$O' = O \ast \delta \tag{A.5}$$

More generally, the recorded image R can be correlated with a single-valued correlation inverse function G [11], that is a function in which the elements of the array are all equal in magnitude, and where the result of the correlation for a point source must, in the ideal case, be an impulse or δ function [11].

A.2 Wavelength

The energy of an electromagnetic wave is given by:

$$E = h_\gamma f_\gamma \tag{A.6}$$

where

E = electromagnetic energy
h_γ = Planck's constant
f_γ = frequency

The wavelength can then be calculated from the energy:

$$c_\gamma = f_\gamma \lambda \tag{A.7}$$

where

c_γ = speed of light in a vacuum
λ = wavelength

At 140 keV, which is the energy of the radioisotope $^{99\mathrm{m}}$Tc, conversion from electron Volts to Joules and use of the constants:

$$\begin{aligned} 1 \text{ eV} &= 1.602 \times 10^{-19} \text{ J} \\ h_\gamma &= 6.626 \times 10^{-34} \text{ J.s} \\ c_\gamma &= 2.998 \times 10^{8} \text{ m/s} \end{aligned}$$

gives a wavelength $\lambda = 8.857 \times 10^{-12}$ m for a vacuum. Note that a ray approximation is only applicable if $\lambda \ll$ than the diameter of a 'pinhole' [48].

A.3 Modified uniformly redundant array generation

A 'basic' MURA of size s, where s is prime, has rows and columns numbered 0 to $s - 1$. The binary matrix elements are [11]:

$$\begin{aligned} &0 \text{ if } i = 0 \\ &1 \text{ if } j = 0, i \neq 0 \\ &1 \text{ if } C_i C_j = +1 \\ &0 \text{ otherwise} \end{aligned} \tag{A.8}$$

where

i = MURA pattern row
j = MURA pattern column
C_q = the general Jacobi Symbol

C_q calculates whether q is a quadratic residue modulo the prime [11]. That is, q is a quadratic residue of s if [17]:

$$z^2 \bmod s = q \bmod s \tag{A.9}$$

where z is a whole number. Note that the sequence repeats for all values of $z > s$, and that $q \bmod s$ is always q for $q < s$.

The resultant C_q is either $+1$ for quadratic residues or -1 for non-residues [11], and matrix elements are symmetric about the diagonal (figure A.1). The MURA becomes pattern-centred if the zero-frequency component of the Fourier transform is shifted to the centre of the spectrum [11]. That is, the $i = 0$ and $j = 0$ constraints generate the central row and column of the aperture pattern (figure A.2), where white indicates open pattern elements.

This 'basic' pattern then forms the centre of, and is repeated to obtain the mosaic aperture pattern [5, 9, 22]. The original quadrants are labelled in black (figure A.3). Repeated quadrants are labelled in grey. Dashed lines represent the central row and column of the pattern, both of which extend from the original aperture into the mosaic. The anti-symmetric pattern is inverted (figures A.4 and A.5). The Fourier transform of the aperture pattern consists of a peak above a uniform plane (figure A.6).

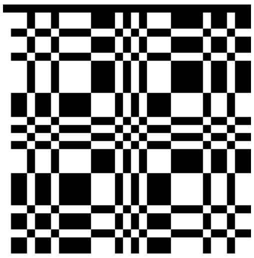

Figure A.1: ‘Basic’ MURA pattern

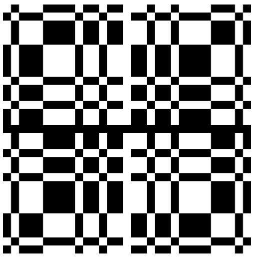

Figure A.2: ‘Basic’ pattern-centred MURA

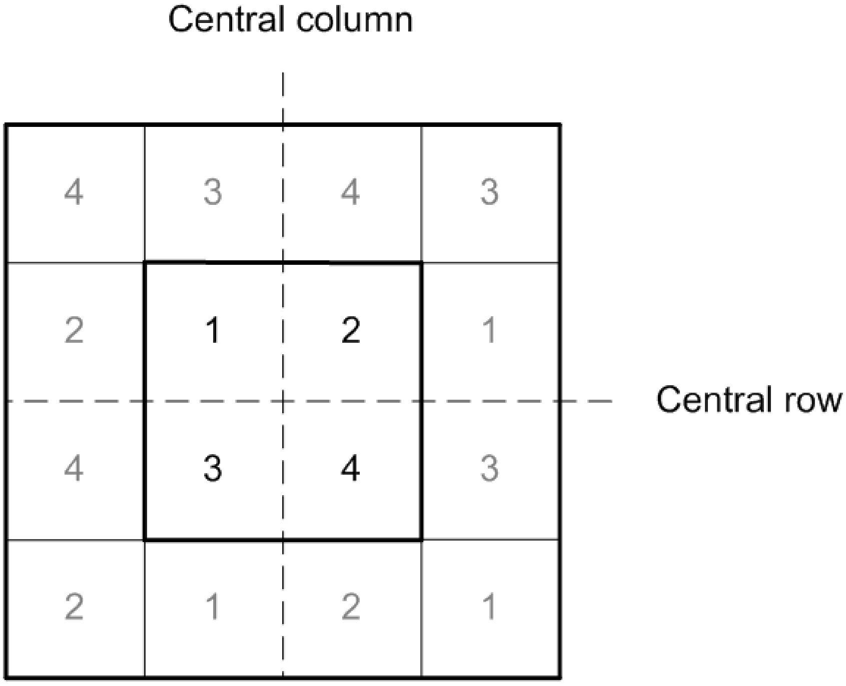

Figure A.3: Schematic of an MURA mosaic

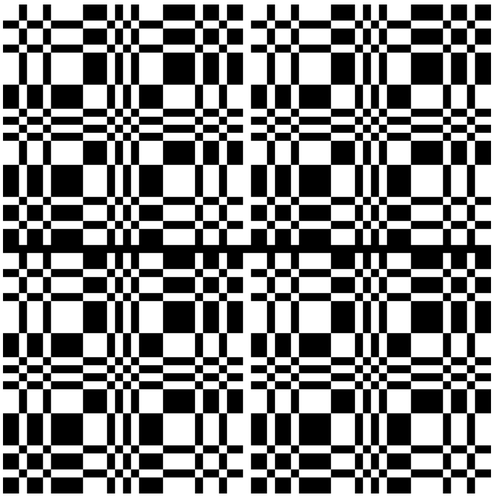

Figure A.4: Mosaic pattern-centred MURA

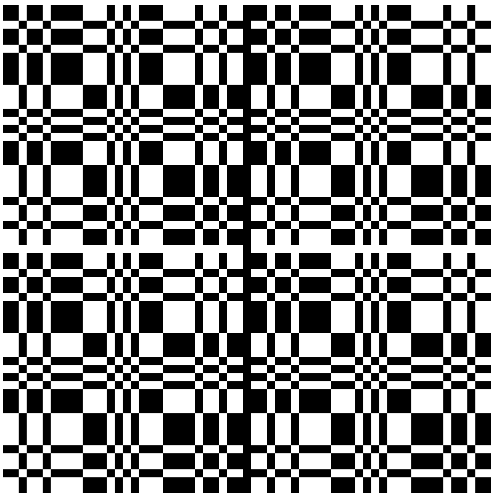

Figure A.5: Mosaic pattern-centred MURA rotated by 90 °

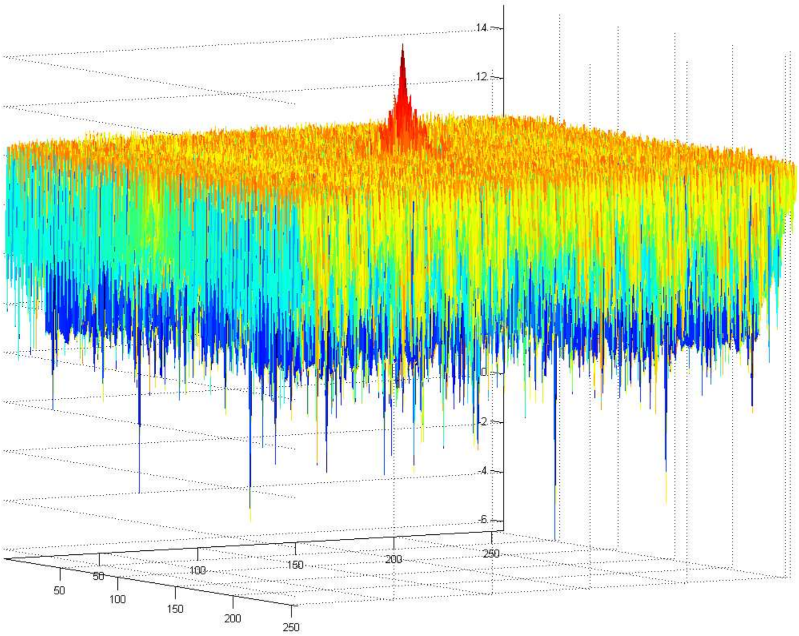

Figure A.6: Fourier transform of a mosaic pattern-centred MURA

A.4 Interpolation

The detector is represented as a discrete array of square pixels of length of side w_d (figure A.7). The point at which the line intersects a particular pixel has, for example, labels u and v relative to the lower left corner of that pixel. A theoretical pixel β of length of side w_d is centred at the point of intersection. Three particular cases of interpolation follow:

1. If the line intersects the pixel centre, $u = v = \frac{1}{2}\, w_d$, and the calculated activity must only be assigned to pixel 1.
2. If the line intersects the boundary between four adjacent pixels, $u = v = w_d$, and one quarter of the calculated activity must be assigned to each of pixels 1 to 4.
3. If $u = \frac{1}{2}\, w_d$ and $v = w_d$, the calculated activity must be distributed equally between pixels 1 and 3.

In the general case, β overlaps adjacent detector pixels. The percentage of calculated activity that is allocated to a particular adjacent pixel is then the product of the percentages by which that pixel overlaps β, on both the x and the y axes.

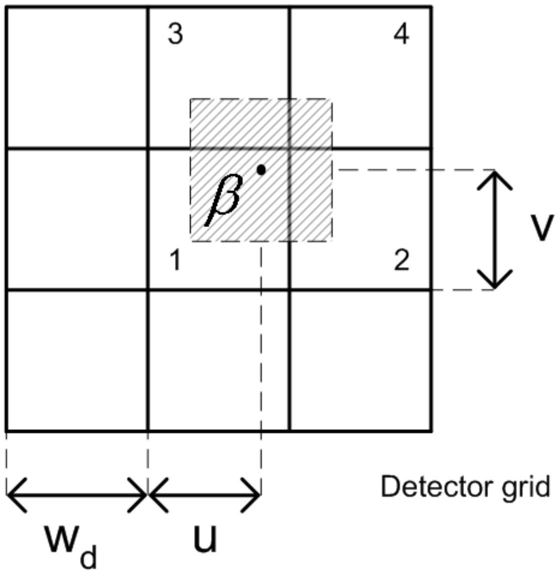

Figure A.7: Schematic of detector grid interpolation

A.5 Single true pinhole approximation

If a detector pixel is located at horizontal distance c from the centre of the aperture pattern (figure A.8), and if the source is at height h_1 above the aperture, which is in turn at height h_2 above the detector, then the corresponding point of the source must be located at horizontal distance d, where:

$$\frac{c}{h_2} = \frac{d}{h_1} \tag{A.10}$$

The physical distance r is then given by:

$$r = \sqrt{(c+d)^2 + (h_1 + h_2)^2} \tag{A.11}$$

The activity measured by a specific pixel of the detector can be corrected in accordance with the inverse square law:

$$\begin{aligned} I_c &= I_m \times 4\pi r^2 \\ &= I_m \times 4\pi \left((c+d)^2 + (h_1+h_2)^2\right) \end{aligned} \tag{A.12}$$

where

I_c = corrected activity
I_m = measured activity

That is, if imaging geometry is known, equation A.10 can be used to calculate d for each specific pixel of the detector, and physical distance used to correct the activity measured.

A.6 Zero-order artifact correction

The correction for zero-order artifacts requires division by a pre-factor, where the pre-factor is given as [18, 22]:

$$\cos^3\left(\arctan\left(\frac{|\vec{r_i}|}{z}\right)\right) \tag{A.13}$$

where for a specific pixel of the detector, $\vec{r_i}$ and z [22] equate to the dimensions $c+d$ and $h_1 + h_2$ respectively (figure A.8). Equation A.13 then becomes:

$$\begin{aligned} & \cos^3 \left(\arctan\left(\frac{c+d}{h_1+h_2}\right)\right) \\ = & \cos^3 \left(\alpha \right) \end{aligned} \tag{A.14}$$

where

α = angle of incidence relative to the system axis

Equation A.14 must be adjusted by the term $\cos(\alpha)$ for ray-tracing as opposed to a flux-based approach. Division by the pre-factor then becomes:

$$\begin{aligned} I_c = & \; I_m \times \frac{1}{\cos^2\left(\alpha\right)} \\ = & \; I_m \times \frac{\left((c+d)^2 + (h_1+h_2)^2\right)}{(h_1+h_2)^2} \end{aligned} \tag{A.15}$$

Relative to equation A.12 (page 74), which is the intuitive correction for physical distance, equation A.15 differs by the factor:

$$4\pi(h_1+h_2)^2 \tag{A.16}$$

which for a planar source parallel to the crystal is constant and does not alter the image.

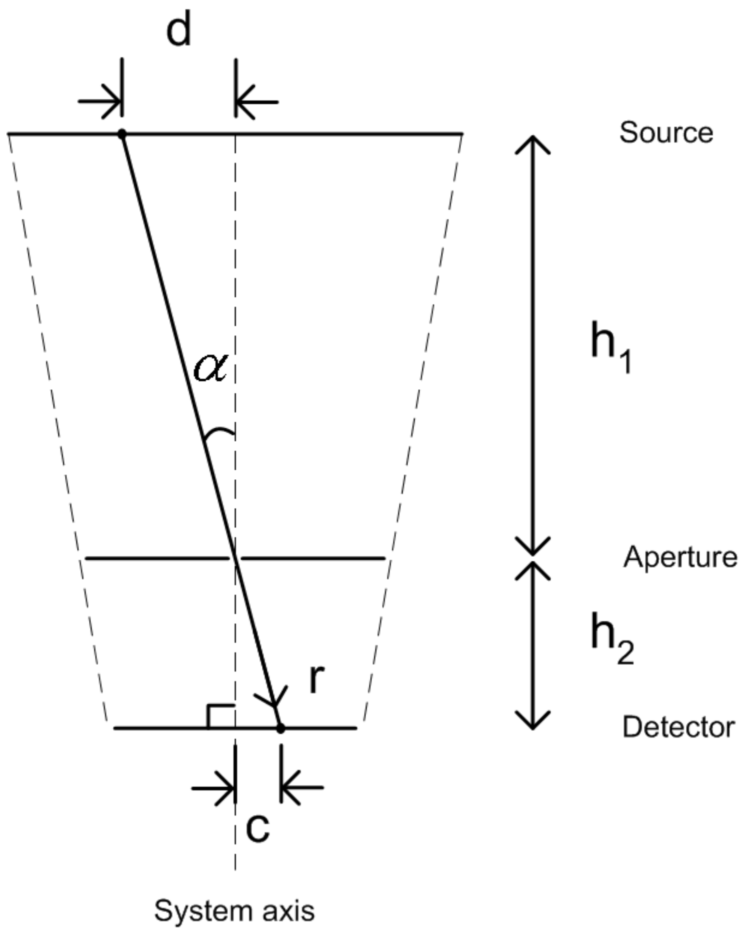

Figure A.8: Schematic of a single true pinhole approximation

A.7 Root-mean-square error measurement

The RMSE measurement is computed over the entire image, and is based on the percentage by which the pixels of the simulated reconstruction differ from the corresponding pixels of the appropriate phantom [49]:

$$e = \frac{\sum_{\forall q} \left(O_q - O_q^{'} \right)^2}{\sum_{\forall q} {O_q}^2} \times 100\ \% \qquad \text{(A.17)}$$

where

e = root-mean-square error
O_q = phantom image intensity at pixel q
$O_q^{'}$ = reconstructed image intensity at pixel q

A.8 Mask anti-mask technique

From equation A.1 (page 66):

$$R_r = O \ast A_r \tag{A.18}$$

where

R_r = the recorded image for a rotated aperture

A_r = the rotated aperture

From equation A.2:

$$O_r^{'} = R_r \otimes G_r \tag{A.19}$$

where

$O_r^{'}$ = the reconstructed image for a rotated aperture

G_r = the decoding array for a rotated aperture

Anti-symmetric MURA inversion is equivalent to a 90 ° rotation of the aperture [19]. That is, A_r is the inverse of A and G_r is the inverse of G. For a binary pattern, where the decoding array has values $+1$ and -1 [11]:

$$G_r = \bar{G} = -G \tag{A.20}$$

From equations A.2 and A.19, the implementation of second-order artifact reduction (section 2.3, page 6) then becomes:

$$\begin{aligned} O' + O_r^{'} &= R \otimes G + R_r \otimes G_r \\ &= R \otimes G + R_r \otimes (-G) \\ &= R \otimes G - R_r \otimes G \\ &= (R - R_r) \otimes G \end{aligned} \tag{A.21}$$

A.9 Basic filters

A Fourier filter can be modelled by:

$$k = l \ast m \tag{A.22}$$

where

$k =$ ideal PSF

$l =$ projected PSF

$m =$ correction factor

Fourier transformation gives:

$$\begin{aligned} \mathcal{F}(k) &= \mathcal{F}(l \ast m) \\ &= \mathcal{F}(l) . \mathcal{F}(m) \end{aligned} \tag{A.23}$$

If the general Fourier transform of q is $\mathcal{F}(q) = Q$, then equation A.23 becomes:

$$\begin{aligned} K &= L.M \\ M &= \frac{K}{L} \end{aligned} \tag{A.24}$$

where M is the transfer function. If the general inverse Fourier transform of Q is $\mathcal{F}^{-1}(Q) = q$, equation A.24 becomes:

$$m = \mathcal{F}^{-1}\left(\frac{K}{L}\right) \tag{A.25}$$

With reference to equation A.22, the ideal corrected projection k' can then be computed if l is replaced with the acquired projection $l\,'$. The technique allows for both the reduction of minor artifacts and the enhancement of resolution, but note that severe non-linear artifacts invalidate the transfer function approximation.

A.10 A general imaging geometry

The intensity I_q at a distance r_q away from a point source S with intensity I_S is given by:

$$I_q = \frac{I_S}{4\pi {r_q}^2} \tag{A.26}$$

The shortest distance between a point source and a square detector is represented by r_x , which is perpendicular to the plane of the detector (figure A.9). The longest possible distance to a point of detection is then represented by r_y :

$$\begin{aligned} r_x &= h && \text{(A.27)} \\ r_y &= \sqrt{h^2 + 2w^2} && \text{(A.28)} \end{aligned}$$

where

h = height of the source above the detector
w = length of side of a square detector

The greatest possible change in I_q on the detector, expressed as a fraction of the maximum I_q , together with equation A.26 becomes:

$$\begin{aligned} \Delta I &= \frac{I_x - I_y}{I_x} && \text{(A.29)} \\ &= \frac{{r_y}^2 - {r_x}^2}{{r_y}^2} && \text{(A.30)} \end{aligned}$$

It becomes useful to work with the ratio h/w. From equations A.27 and A.28, ΔI expressed as a percentage becomes:

$$\Delta I = \frac{2}{\left(\frac{h}{w}\right)^2 + 2} \times 100\,\% \tag{A.31}$$

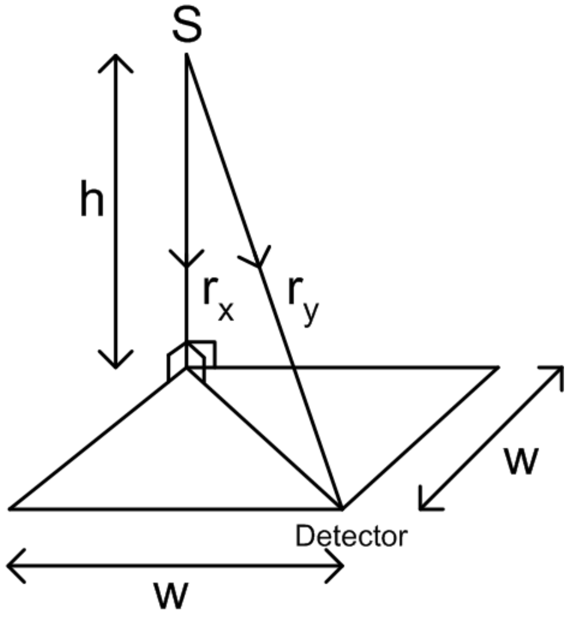

Figure A.9: Schematic of a general imaging geometry

A.11 A realistic imaging geometry

There can be no attenuation at the shortest distance between the source and the detector. At the longest possible distance to a point of detection, the attenuation of r_y is a function of both system geometry and the properties of the aperture material (figures A.10 and A.11):

$$t = e^{-\rho\mu r_m} \tag{A.32}$$

where

t = aperture material transmission
ρ = aperture material density
μ = aperture material attenuation coefficient
r_m = effective thickness of the aperture material

where μ is the attenuation coefficient at the energy of interest.

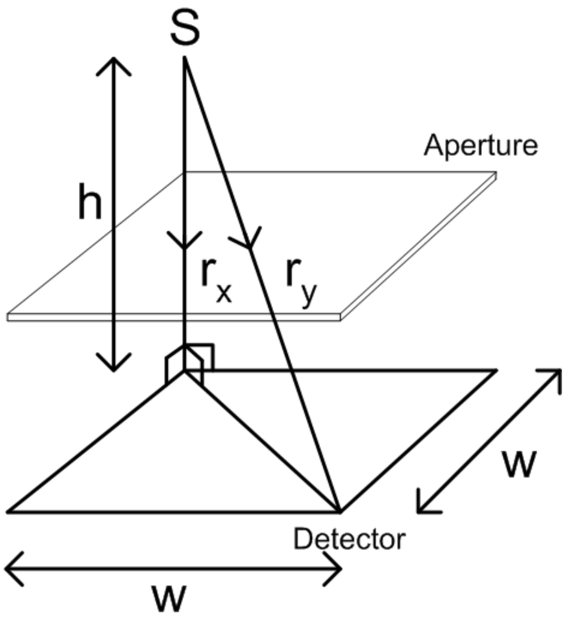

Figure A.10: Schematic of a general imaging geometry and realistic aperture

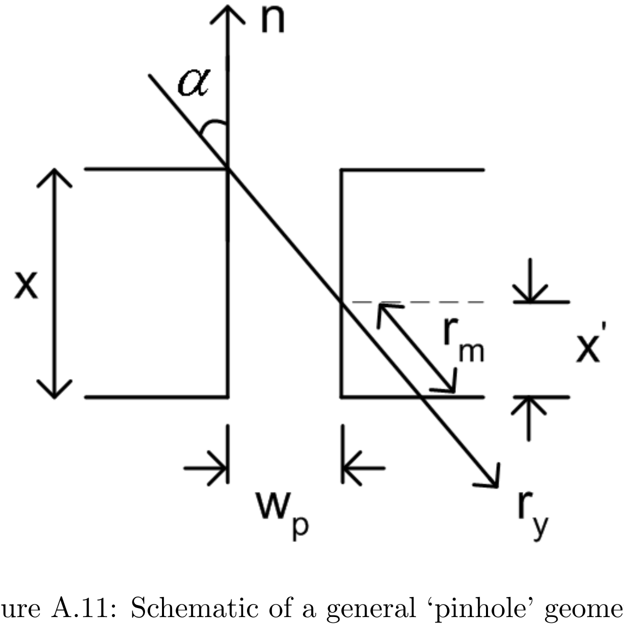

Figure A.11: Schematic of a general ‘pinhole’ geometry

From equation A.29 (page 79), the inclusion of aperture transmission together with equation A.26 gives:

$$\begin{aligned} \Delta I &= \frac{I_x - I_y t}{I_x} \\ &= \frac{{r_y}^2 - {r_x}^2 t}{{r_y}^2} \end{aligned} \tag{A.33}$$

From equations A.27, A.28, and A.32, ΔI expressed as a percentage becomes:

$$\Delta I = \frac{\left(\frac{h}{w}\right)^2 + 2 - \left(\frac{h}{w}\right)^2 e^{-\rho\mu r_m}}{\left(\frac{h}{w}\right)^2 + 2} \times 100\,\% \tag{A.34}$$

From figure A.11:

$$r_m = \frac{x'}{\cos\alpha} \tag{A.35}$$

$$x' = x - \frac{w_p}{\tan\alpha} \tag{A.36}$$

where

x = aperture material thickness

w_p = ‘pinhole’ width

The unit normal n is perpendicular to the aperture, and the aperture is parallel to the detector. From figure A.10:

$$\alpha = \arctan\left(\frac{\sqrt{2w^2}}{h}\right) \tag{A.37}$$

From equations A.35, A.36 and A.37:

$$r_m = \sqrt{1 + 2\left(\frac{h}{w}\right)^{-2}} \left[x - \frac{w_p}{\sqrt{2}}\left(\frac{h}{w}\right)\right] \tag{A.38}$$

where r_m must be $\geqslant 0$.

A.12 Point spread function

If R is the simulated multiplexed data, and PSF is the point spread function of the detector, then the blurred data R' is obtained by means of convolution:

$$R' = R \ast PSF \tag{A.39}$$

where PSF is a normalised Gaussian distribution with standard deviation σ.

A.13 Aperture attenuation

From equation A.32 (page 80), if a gamma-ray is incident perpendicular to the aperture material:

$$\begin{aligned} a &= 1 - t \\ &= 1 - e^{-\rho\mu x} \end{aligned} \tag{A.40}$$

where

a = aperture material attenuation

For example, at 140 keV, which is the energy of $^{99\mathrm{m}}$Tc, the physical attenuation properties of the materials tungsten and lead are:

Tungsten: $\rho = 19.3\ \mathrm{g/cm^3}$
$\mu = 1.76\ \mathrm{cm^2/g}$

Lead: $\rho = 11.35\ \mathrm{g/cm^3}$
$\mu = 2.37\ \mathrm{cm^2/g}$

A.14 Basic statistics

A Gaussian approximation can be used in place of the Poisson distribution, provided that the average number of counts is > 15 [22]. The altered number of counts ${I_m}'$ acquired by a specific pixel of the detector is given by:

$$ {I_m}' = I_m + \left(\sqrt{I_m} \times N\right) \tag{A.41} $$

where

$N =$ normally distributed random number

and where ${I_m}'$ must be a whole number.

A.15 Design efficiency

An array of limited-FOV coded apertures that contains n_a individual apertures gives $1/n_a$ the activity at the detector. That is, a specific point of the source illuminates only a single limited FOV.

Thin aperture material simplifies the construction of patterns that are not self-supporting. If an opaque self-supporting pattern has an open fraction f_1, and an opaque non-self-supporting pattern has an open fraction f_2, use of the latter increases activity at the detector by f_2/f_1.

A highly transparent aperture material of attenuation a_1, as opposed to an opaque material of attenuation a_2, must give a_2/a_1 times the activity at the detector. However, this is only applicable to the closed fraction of the aperture pattern, $1 - f_2$.

Smaller pattern elements reduce the count statistics of the reconstructed image, but do not alter activity at the detector. A source positioned at a fraction $1/h$ of the distance increases the activity at the detector by h^2.

An ultra-near-field design that incorporates each of the independent theoretical advances then gives the change in activity at the detector $\Delta I'$ as:

$$ \Delta I' = \frac{1}{n_a} \, \frac{f_2}{f_1} \, \frac{a_2}{a_1} \, (1 - f_2) \, h^2 \tag{A.42} $$

The change in bit-depth Δb of the gamma camera acquisition is then given by:

$$\Delta b = \frac{\ln\left(\Delta I'\right)}{\ln 2} \tag{A.43}$$

For example, as opposed to a single coded aperture, a 3 × 3 array of limited-FOV coded apertures allows for near-field artifact reduction. Relative to a tungsten sheet of thickness 1 mm, 100 μm thick tungsten foil allows for the reduction of thickness artifacts.

An MURA pattern has an open fraction of 50 % [11]. By contrast, an NTHT implementation attains an open fraction of only 12.5 % [19]. A 1 × 1, as opposed to a 2 × 2 detector pixel area projection does not alter the open fraction of the aperture material.

At one quarter the distance, use of equations A.42 and A.43 gives $\Delta I' = 11.89$, or an additional 3.57 bits of data. That is, unless limited by the count rate of the gamma camera, system sensitivity can be improved.

A.16 Laser alignment

A spirit level can be used to ensure that both the base of the frame and the upper surface of the tripod mechanism are level and therefore parallel. If second-order artifact reduction is to be implemented by means of a 90 ° rotation of the aperture, the centre of the aperture pattern must be aligned with the centre of rotation of the aluminium frame. A laser that generates a ‘cross’ pattern can be positioned above the frame, and an iterative methodology used:

1. The centre of the beam is marked on paper that is attached to the aperture surface. The process is repeated for multiple aperture rotations.
2. The laser is shifted so that the centre of the beam corresponds to the centre of the multiple marks.
3. Points 1 and 2 are repeated until the centre of the beam corresponds to the centre of rotation. That is, only a single point is marked, which does not move relative to the beam. The laser position is then fixed and the paper removed.

4. The aperture is shifted, so that the centre of the aperture pattern corresponds to the centre the beam (figure A.12). Further, it can be ensured that the central row and column of the aperture pattern are accurately and fully illuminated by the laser, both at the 0 ° and 90 ° aperture rotations.

Note that a specific coded aperture is aligned for use with a specific aperture carriage. An aperture and carriage pair can then be installed with repeatability.

A.17 Aperture design

If a 'basic' MURA pattern is of size s, where s is prime, the mosaic version of the pattern [5, 9] is of size $(2s-1)$, as the central row and column of the aperture pattern are not repeated (appendix A.3, page 68). Similarly, if an MURA pattern is of size s', the NTHT implementation of the same pattern [14, 15, 16] is of size $(2s'-1)$, as supporting rows and columns must be inserted between all pattern elements.

If w_p is the physical element or aperture hole width, then for a mosaic NTHT pattern:

$$y = w_p \left(2\left(2s-1\right)-1\right) \tag{A.44}$$

$$s_m = \left(\left(\frac{y_m}{w_p}+1\right)\frac{1}{2}+1\right)\frac{1}{2} \tag{A.45}$$

where

y = physical aperture length of side
y_m = maximum physical aperture length of side
s_m = maximum 'basic' MURA pattern size

where s_m must be a whole number.

The Philips Axis has pixels of size 1.167315 mm × 1.167315 mm. At a 1:1 imaging ratio, the illumination of a 2×2 detector pixel area requires coded aperture holes that are of at least the same area as a single detector pixel. Square holes of $w_p = 1.2$ mm are used, which for a 200 mm × 200 mm sheet of aperture material gives $s_m = 42$.

The possible primes in descending order are then:

41, but the resultant pattern is symmetric

37, but the pattern is again symmetric

and 31, with an anti-symmetric pattern

That is, the mosaic aperture pattern contains 61 elements, and the NTHT implementation contains 121 elements (figure A.13). The FOV is then $y = 145.2$ mm × 145.2 mm.

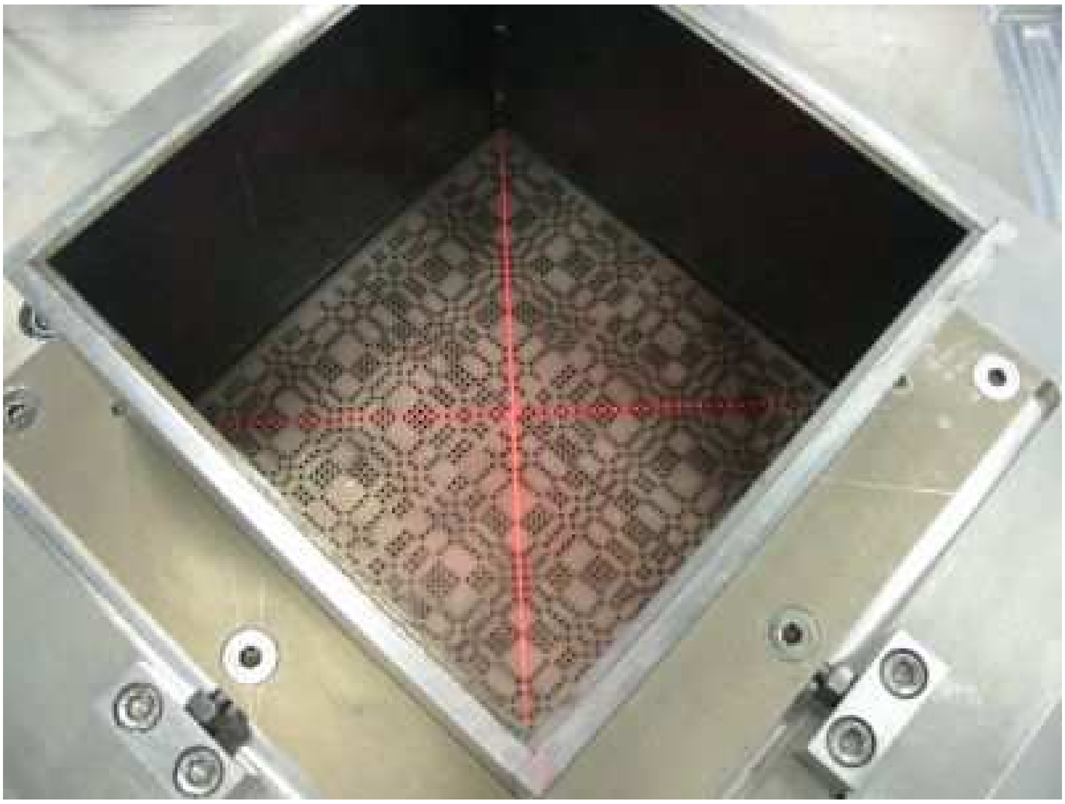

Figure A.12: Laser with ‘cross’ beam used for aperture pattern alignment

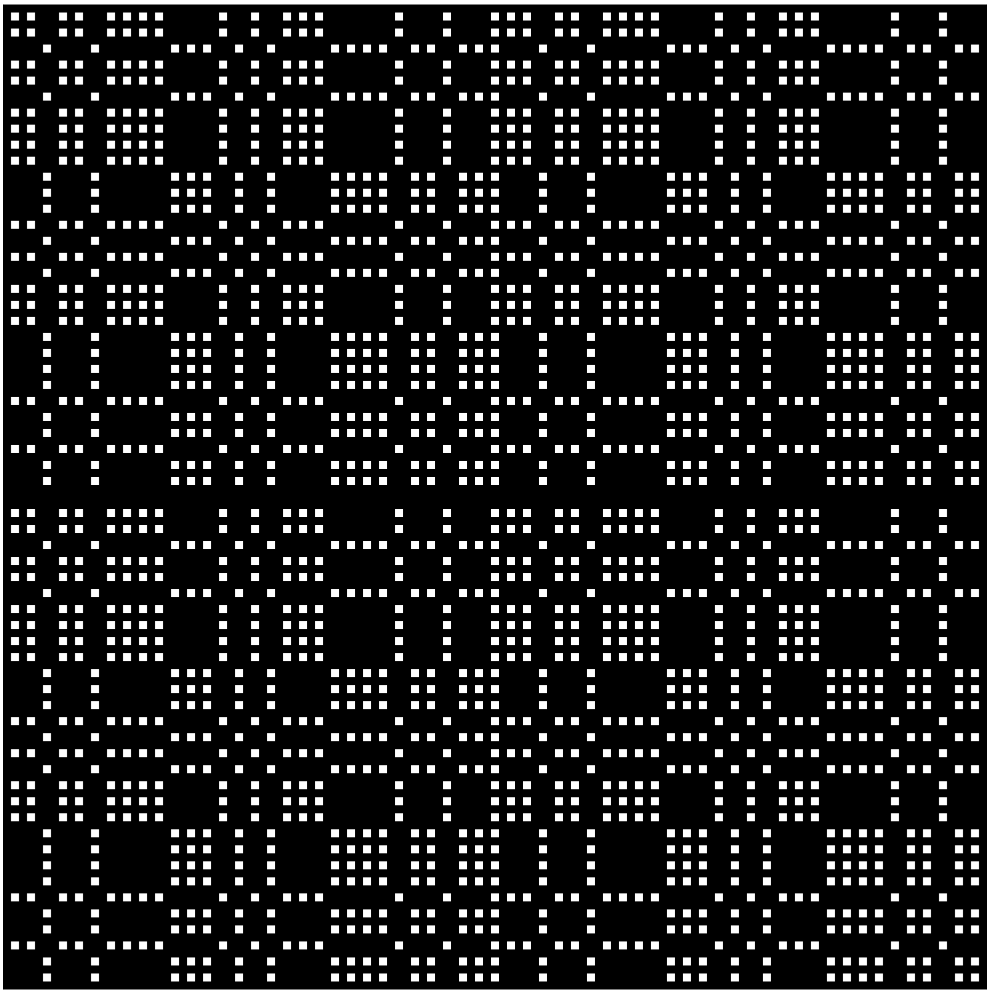

Figure A.13: NTHT implementation of a mosaic pattern-centred MURA

Appendix B

Schematics

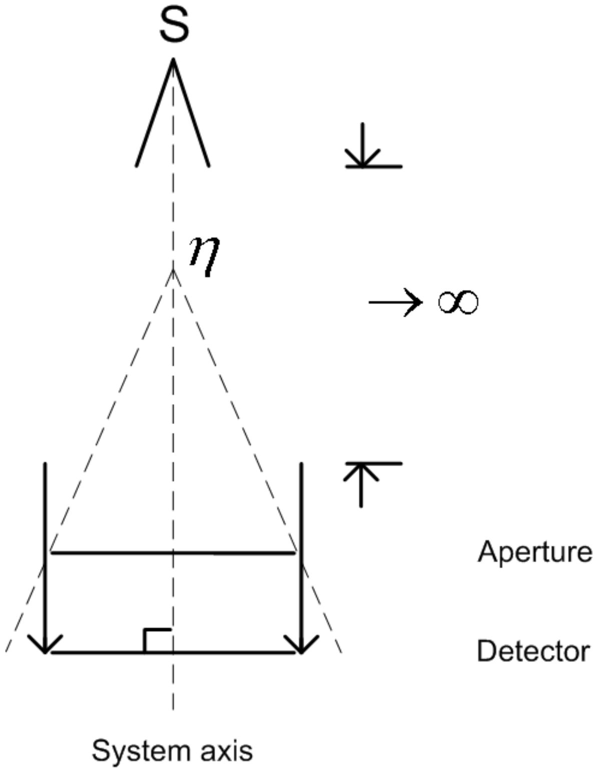

Figure B.1: Schematic of a box camera with a point source at ∞

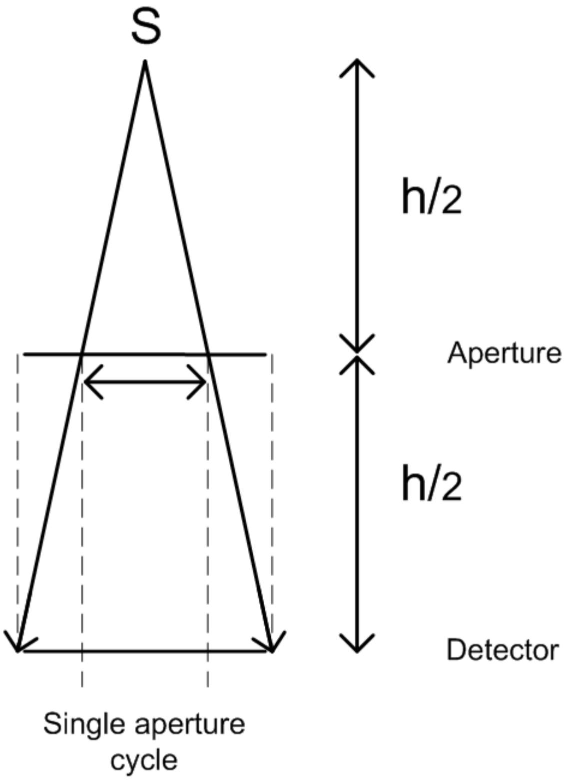

Figure B.2: Schematic of a box camera at a 1:1 imaging ratio

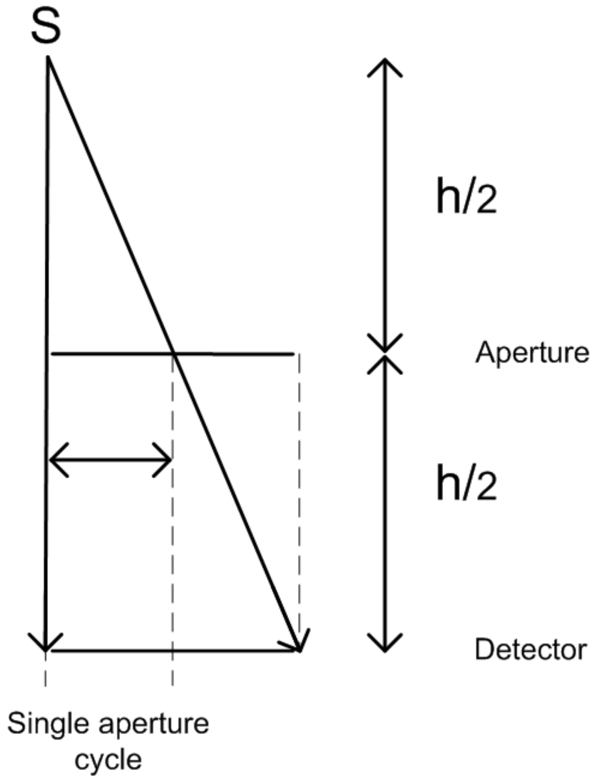

Figure B.3: Schematic of a single mosaic aperture cycle projection

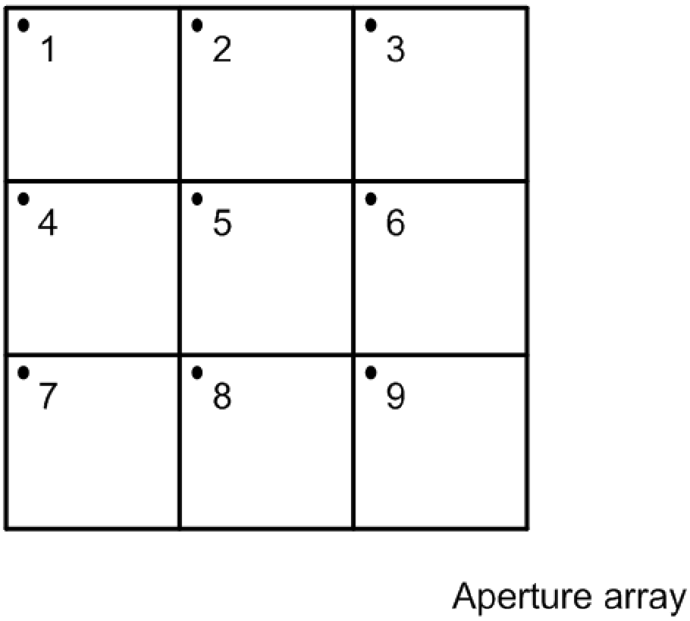

Figure B.4: Schematic of an array of coded apertures

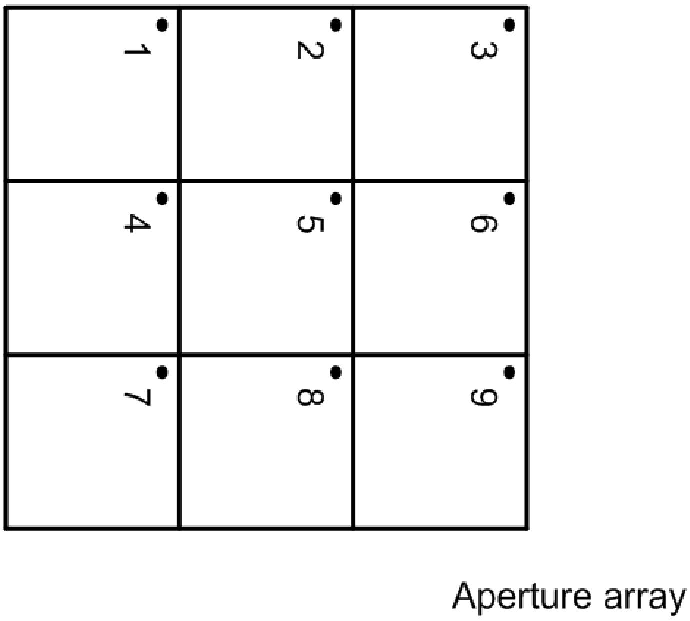

Figure B.5: Schematic of an array of coded apertures, individually rotated

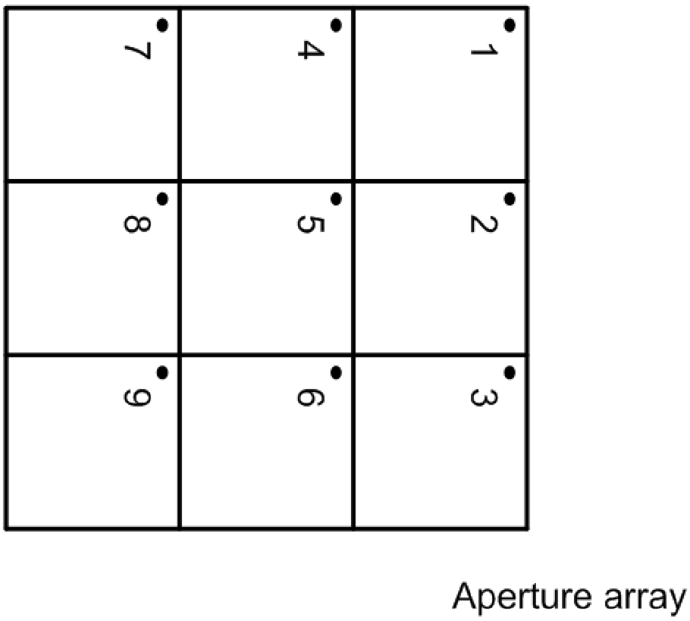

Figure B.6: Schematic of an array of coded apertures, rotated in entirety

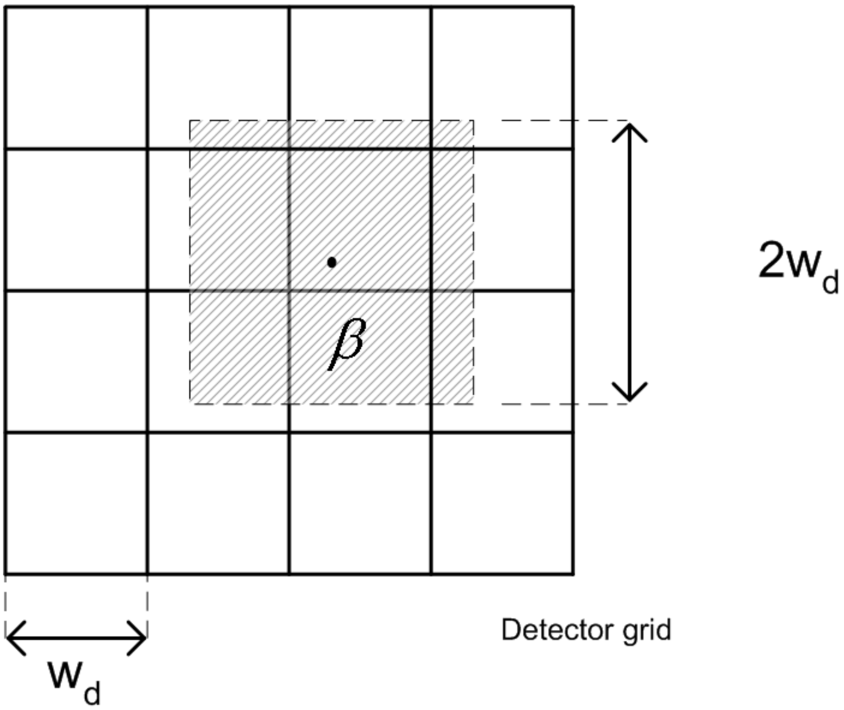

Figure B.7: Schematic of detector grid interpolation, 2 × 2 area projection

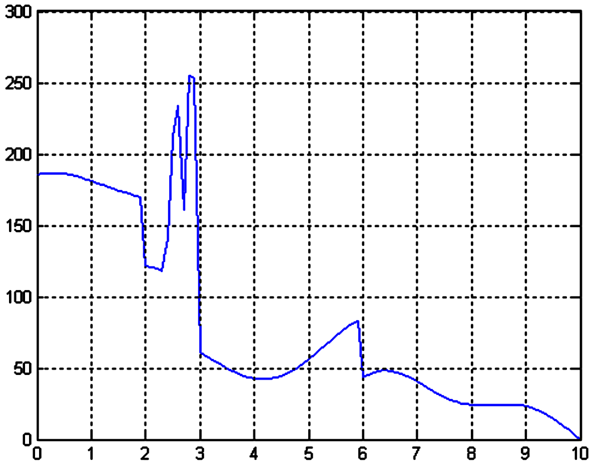

Figure B.8: Schematic of an original sample signal

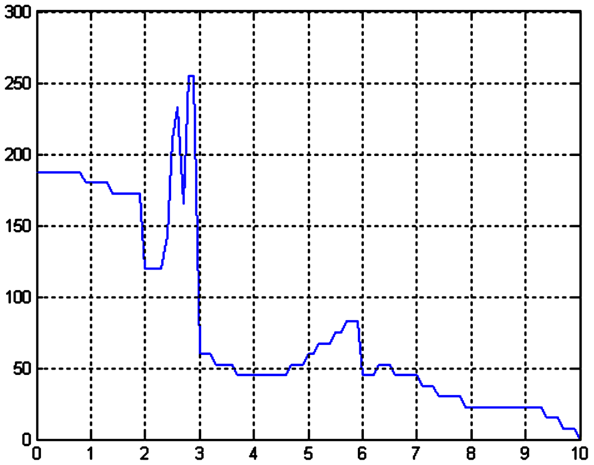

Figure B.9: Schematic of sample signal with a 5-bit vertical resolution

Appendix C

Simulated images

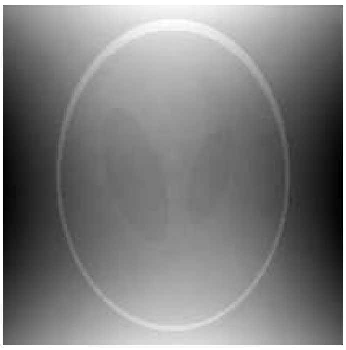

Figure C.1: Simulated near-field reconstruction

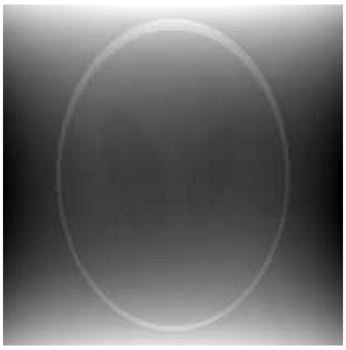

Figure C.2: Simulated near-field reconstruction with zero-order correction

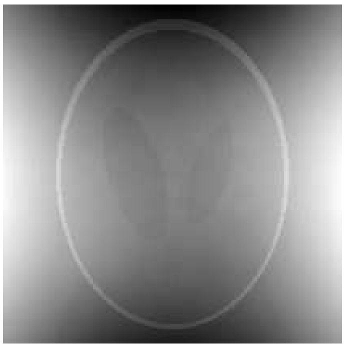

Figure C.3: Simulated near-field reconstruction, rotated coded aperture

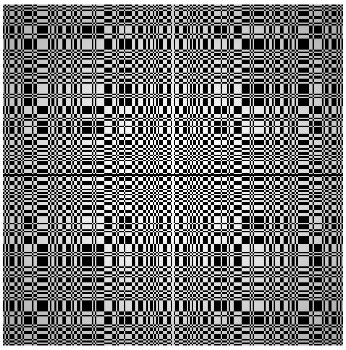

Figure C.4: Simulated point source projection

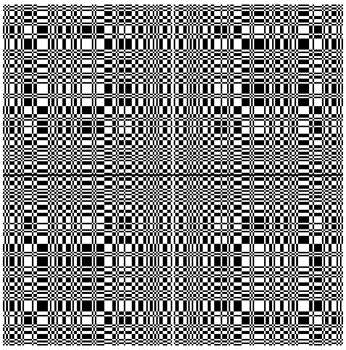

Figure C.5: Ideal point source projection

Figure C.6: Simulated point source reconstruction

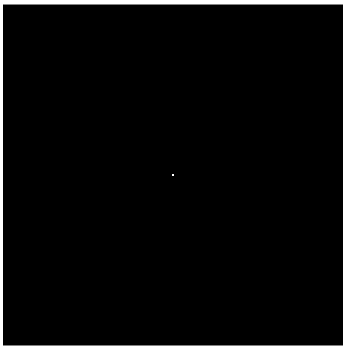

Figure C.7: Ideal point source reconstruction

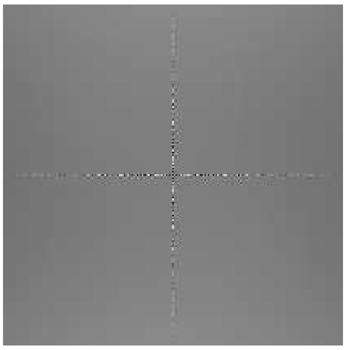

Figure C.8: Subtraction of ideal and simulated point source reconstructions

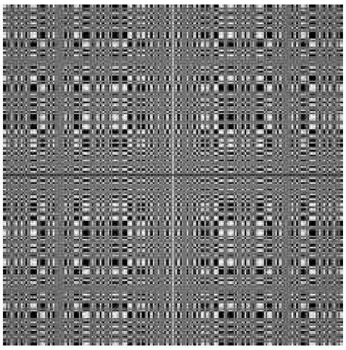

Figure C.9: Simulated point source projection at 2× the distance

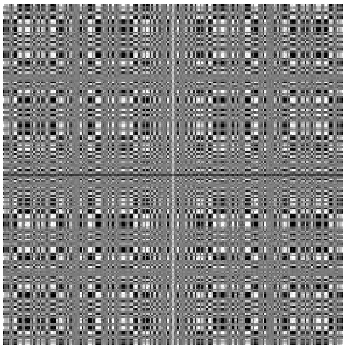

Figure C.10: Simulated point source projection at 4× the distance

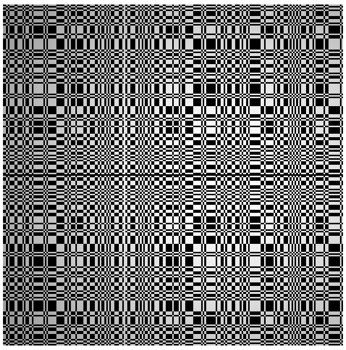

Figure C.11: Simulated projection of a shifted point source

Figure C.12: Low contrast Shepp-Logan phantom

Appendix D

Photographs

Figure D.1: Gamma camera side of the coded aperture frame

Figure D.2: Circular bearing in the base of the coded aperture frame

Figure D.3: Plate constructed to match the circular bearing

Figure D.4: Rotation stage with circular bearing plate in position

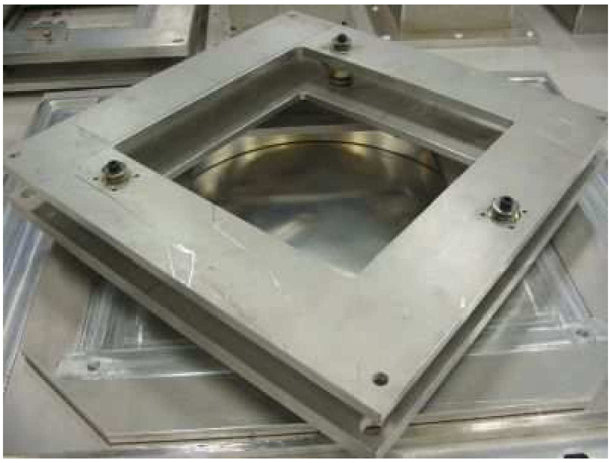

Figure D.5: Tripod mechanism with adjustable plates

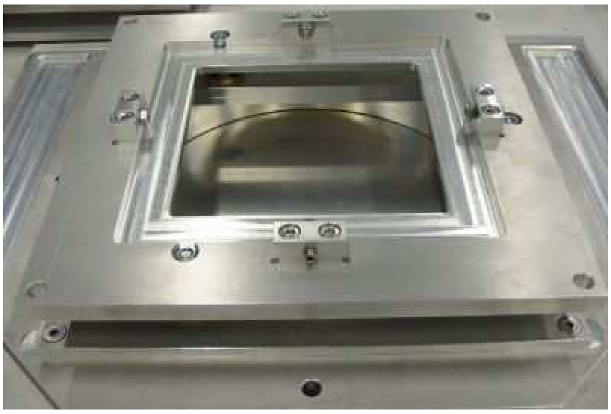

Figure D.6: The aperture carriage bolted onto the rotation stage

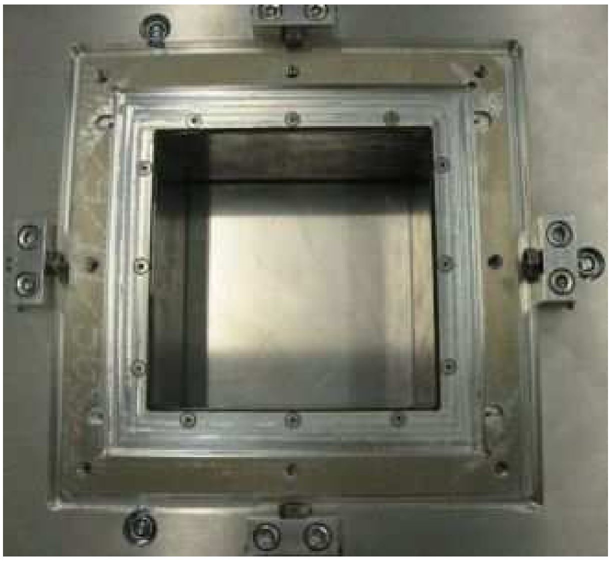

Figure D.7: Lower half of a lead 'tube'

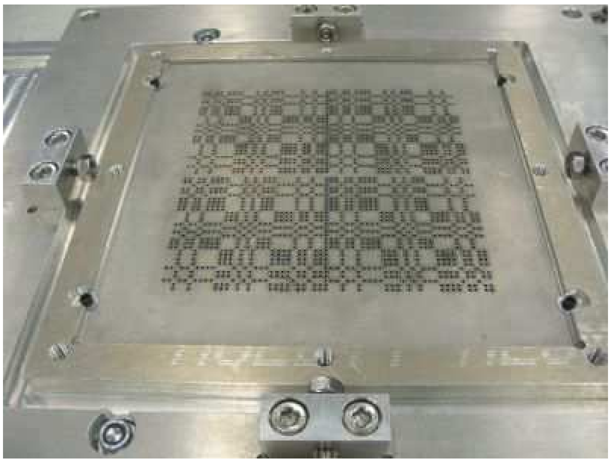

Figure D.8: Coded aperture installed in the lower lead ‘tube’

Figure D.9: Complete frame with upper and lower lead ‘tubes’

Figure D.10: Laser drilling of a 1 mm tungsten sheet

Figure D.11: 2D printed ink and $^{99\mathrm{m}}$Tc Shepp-Logan phantom

Figure D.12: 2D printed ink and $^{99\mathrm{m}}$Tc bar phantom

Appendix E

Tables

Table E.1: Column label descriptions for table E.2

Short description	**Full column description**
Figure	figure number
Near-field	use of a near-field geometry
Corrected	use of 2nd-order artifact correction
Thickness	model includes aperture material thickness
Attenuation	model includes aperture material attenuation
Hole width	model includes 'pinhole' widths
Quantization	model includes gamma camera digitization effects
Statistics	model includes radioactivity count statistics
PSF	model includes gamma camera PSF
Array	use of an array of coded apertures
Optimal	use of a high-resolution projection
Transparent	use of a high-transparency coded aperture
Comments	additional comments
RMSE	root-mean-square error measurement (%)

Table E.2: Comparison of the features of the primary simulated images

Figure	**Near-field**	**Corrected**	**Thickness**	**Attenuation**	**Hole width**	**Quantization**	**Statistics**	**PSF**	**Array**	**Optimal**	**Transparent**	**Comments**	**RMSE**
4.4													3
4.5												zero-order correction	0.02
4.6	●	●											25
4.7	●	●										2× distance	3
4.8	●	●										4× distance	0.3
5.3	●								●				136
5.4	●								●			rotated	117
5.5	●	●							●				2
5.7	●	●	●	●	●								39
5.8	●	●	●	●	●				●				62
5.9	●	●	●	●	●				●				46
5.10	●	●	●	●	●				●			contrast-shifted	7
5.15	●	●			●					●			
5.16	●	●			●					●			23
5.17	●	●			●								28
5.18	●	●			●			●		●			25
5.19	●	●			●			●					34
5.21	●	●	●	●	●	●						8-bit	47
5.22	●	●	●	●	●	●					●	8-bit	94
5.23	●	●	●	●	●	●						16-bit	42
5.24	●	●	●	●	●	●					●	16-bit	20
5.26	●	●	●	●	●	●	●				●	8-bit	
5.27	●	●	●	●	●	●	●				●	13-bit	
5.28	●	●	●	●	●	●	●				●	16-bit	
5.29	●	●	●	●	●	●	●					self-supporting	62
5.30		●	●	●	●	●	●					self-supporting	239
5.31	●	●	●	●	●	●	●		●	●	●		96
5.32		●	●	●	●	●	●		●	●	●		39
C.1	●												303
C.2	●											zero-order correction	262
C.3	●											rotated	422
C.6	●												

Table E.3: Gamma camera sensitivity for the 29 % attenuation aperture

Source Activity		**Count Rate**
(MBq)	**(μCi)**	**(10^3 cps)**
3.1	85	41.3
3.7	100	48.8
12.5	339	111.4
22.1	598	129.0
24.4	660	123.0
37.8	1021	108.1
78.1	2110	41.6

Appendix F

List of publications and patents

The following is a list of the publications and patents arising from this thesis:

1. D. M. Starfield, D. M. Rubin and T. Marwala, "A geometric method for near-field artifact reduction in planar coded aperture nuclear medicine imaging," in *IFMBE Proceedings of the 3rd European Medical and Biological Engineering Conference*, vol. 11, Prague, November 2005, paper 2488.
2. D. M. Starfield, D. M. Rubin and T. Marwala, "Near-field artifact reduction using realistic limited-field-of-view coded apertures in planar nuclear medicine imaging," in *IFMBE Proceedings of the World Congress on Medical Physics and Biomedical Engineering*, vol. 14, Seoul, August 2006, pp. 2198–2202.
3. D. M. Starfield, D. M. Rubin and T. Marwala, "Sampling considerations and resolution enhancement in ideal planar coded aperture nuclear medicine imaging," in *IFMBE Proceedings of the 11th Mediterranean Conference on Medical and Biological Engineering and Computing*, vol. 16, Ljubljana, June 2007, pp. 806–809.
4. D. M. Starfield, D. M. Rubin and T. Marwala, "High transparency coded apertures in planar nuclear medicine imaging," in *Proceedings of the 29th Annual International Conference of the IEEE EMBS*, Lyon, August 2007, pp. 4468–4471.
5. D. M. Starfield, D. M. Rubin, T. Marwala and R. J. Keddy, "High-transparency coded apertures in planar nuclear medicine imaging: experimental results," in *IEEE Nuclear Science Symposium Conference Record*, vol. 4, Honolulu, October 2007, pp. 3151–3154.

6. D. M. Starfield, D. M. Rubin and T. Marwala, "Design of an ultra-near-field system for planar coded aperture nuclear medicine imaging," in *IFMBE Proceedings of the 14th Nordic-Baltic Conference on Biomedical Engineering and Medical Physics*, vol. 20, Riga, June 2008, pp. 590–593.
7. D. M. Starfield, D. M. Rubin and T. Marwala, "Method and apparatus for radiation imaging," International Patent Application WO 2007/054769 A2, May, 2007.
8. D. M. Starfield, D. M. Rubin and T. Marwala, "Coded aperture masks for radiation-based medical imaging," International Patent Application WO 2008/142543 A1, November, 2008.

References

[1] S. R. Cherry, J. A. Sorenson, and M. E. Phelps, *Physics in nuclear medicine*, 3rd ed. Philadelphia: Saunders, 2003.

[2] R. Accorsi, F. Gasparini, and R. C. Lanza, "A coded aperture for high-resolution nuclear medicine planar imaging with a conventional anger camera: experimental results," *IEEE Transactions on Nuclear Science*, vol. 48, no. 6, pp. 2411–2417, 2001.

[3] B. Aschenbach, "X-ray telescopes," *Reports on Progress in Physics*, vol. 48, no. 5, pp. 579–629, 1985.

[4] E. E. Fenimore, "Time-resolved and energy-resolved coded aperture images with URA tagging," *Applied Optics*, vol. 26, no. 14, pp. 2760–2769, 1987.

[5] E. E. Fenimore, "Coded aperture imaging: predicted performance of uniformly redundant arrays," *Applied Optics*, vol. 17, no. 22, pp. 3562–3570, 1978.

[6] L. Mertz and N. O. Young, "Fresnel transformations of images," in *Proceedings of the International Conference on Optical Instruments and Techniques*, 1961, pp. 305–310.

[7] M. L. McConnell, D. J. Forrest, E. L. Chupp, and P. P. Dunphy, "A coded aperture gamma ray telescope," *IEEE Transactions on Nuclear Science*, vol. 29, no. 1, pp. 155–159, 1982.

[8] W. R. Cook, M. Finger, T. A. Prince, and E. C. Stone, "Gamma-ray imaging with a rotating hexagonal uniformly redundant array," *IEEE Transactions on Nuclear Science*, vol. 31, no. 1, pp. 771–775, 1984.

[9] E. Caroli, J. B. Stephen, G. Di Cocco, L. Natalucci, and A. Spizzichino, "Coded aperture imaging in X- and gamma-ray astronomy," *Space Science Reviews*, vol. 45, pp. 349–403, 1987.

[10] T. M. Cannon and E. E. Fenimore, "Tomographical imaging using uniformly redundant arrays," *Applied Optics*, vol. 18, no. 7, pp. 1052–1057, 1979.

[11] S. R. Gottesman and E. E. Fenimore, “New family of binary arrays for coded aperture imaging,” *Applied Optics*, vol. 28, no. 20, pp. 4344–4352, 1989.

[12] J. in ’t Zand. (1996) Coded aperture imaging in high-energy astronomy. Laboratory for High-Energy Astrophysics (LHEA) – Goddard Space Flight Center (GSFC). Last date of access: 13 November 2008. [Online]. Available: astrophysics.gsfc.nasa.gov/cai/coded_intr.html

[13] K. Coolsaet. (1997) Cyclic difference sets. Inference Group, Department of Physics, University of Cambridge. Last date of access: 14 November 2008. [Online]. Available: www.inference.phy.cam.ac.uk/cds/index.htm

[14] E. E. Fenimore, “Coded aperture imaging: the modulation transfer function for uniformly redundant arrays,” *Applied Optics*, vol. 19, no. 14, pp. 2465–2471, 1980.

[15] E. E. Fenimore and T. M. Cannon, “Uniformly redundant arrays: digital reconstruction methods,” *Applied Optics*, vol. 20, no. 10, pp. 1858–1864, 1981.

[16] R. Accorsi, F. Gasparini, and R. C. Lanza, “Optimal coded aperture patterns for improved SNR in nuclear medicine imaging,” *Nuclear Instruments and Methods in Physics Research*, vol. A 474, pp. 273–284, 2001.

[17] D. Calabro and J. K. Wolf, “On the synthesis of two-dimensional arrays with desirable correlation properties,” *Information and Control*, vol. 11, pp. 537–560, 1968.

[18] R. Accorsi and R. C. Lanza, “Near-field artifact reduction in planar coded aperture imaging,” *Applied Optics*, vol. 40, no. 26, pp. 4697–4705, 2001.

[19] D. Schellingerhout, R. Accorsi, U. Mahmood, J. Idoine, R. C. Lanza, and R. Weissleder, “Coded aperture nuclear scintigraphy: a novel small animal imaging technique,” *Molecular Imaging*, vol. 1, no. 4, pp. 344–353, 2002.

[20] O. I. Vassilieva and R. C. Chaney, “Method for reducing background artifacts from images in single-photon emission computed tomography with a uniformly redundant array coded aperture,” *Applied Optics*, vol. 41, no. 7, pp. 1454–1461, 2002.

[21] H. H. Barrett, “Fresnel zone plate imaging in nuclear medicine,” *Journal of Nuclear Medicine*, vol. 13, no. 6, pp. 382–385, 1972.

[22] R. Accorsi, “Design of near-field coded aperture cameras for high-resolution medical and industrial gamma-ray imaging,” Ph.D. dissertation, Massachusetts Institute of Technology, 2001.

[23] A. Steinbach and A. Macovski, "Improved depth resolution with one-dimensional coded aperture imaging," *Journal of Physics D: Applied Physics*, vol. 12, pp. 2079–2099, 1979.

[24] P. P. Dunphy, M. L. McConnell, A. Owens, E. L. Chupp, D. J. Forrest, and J. Googins, "A balloon-borne coded aperture telescope for low-energy gamma-ray astronomy," *Nuclear Instruments and Methods in Physics Research*, vol. A 274, pp. 362–379, 1989.

[25] M. M. Rogulski, H. B. Barber, H. H. Barrett, R. L. Shoemaker, and J. M. Woolfenden, "Ultra-high-resolution brain SPECT imaging: simulation results," *IEEE Transactions on Nuclear Science*, vol. 40, no. 4, pp. 1123–1129, 1993.

[26] S. Berrim, A. Lansiart, and J.-L. Moretti, "Implementing of maximum likelihood in tomographical coded aperture," in *IEEE Proceedings of the International Conference on Image Processing*, vol. 1, 1996, pp. 745–748.

[27] Y.-H. Liu, A. Rangarajan, D. Gagnon, M. Therrien, A. J. Sinusas, F. J. T. Wackers, and I. G. Zubal, "A novel geometry for SPECT imaging associated with the EM-type blind deconvolution method," *IEEE Transactions on Nuclear Science*, vol. 45, no. 4, pp. 2095–2101, 1998.

[28] R. C. Lanza, R. Accorsi, and F. Gasparini, "Coded aperture imaging," U.S. Patent 6,737,652 B2, May, 2004.

[29] R. C. Chaney and O. Vassilieva, "Method and system for reducing background artifacts from uniformly redundant array collimators in single photon emission computed tomography," U.S. Patent 6,580,939 B1, June, 2003.

[30] A. C. Chamberlain, "Determination of an optimum wire mesh collimator and digital filter using monte-carlo simulation," Ph.D. dissertation, Medical University of Southern Africa, 2002.

[31] R. Accorsi and R. C. Lanza, "High-sensitivity dynamic coded aperture imaging," in *IEEE Nuclear Science Symposium Conference Record*, vol. 3, Prague, January 2003, pp. 1833–1837.

[32] M. Gmar, O. Gal, C. Le Goaller, O. P. Ivanov, V. N. Potapov, V. E. Stepanov, F. Lainé, and F. Lamadie, "Development of coded-aperture imaging with a compact gamma camera," *IEEE Transactions on Nuclear Science*, vol. 51, no. 4, pp. 1682–1687, 2004.

[33] R. Accorsi, M. Autiero, L. Celentano, P. Laccetti, R. C. Lanza, M. Marotta, G. Mettivier, M. C. Montesi, P. Riccio, G. Roberti, and P. Russo, "Toward

a Medipix2 coded aperture gamma microscope," in *IEEE Nuclear Science Symposium Conference Record*, vol. 4, 2004, pp. 2461–2464.

[34] Z. Mu and Y.-H. Liu, "Aperture collimation correction and maximum-likelihood image reconstruction for near-field coded aperture imaging of single photon emission computerized tomography," *IEEE Transactions on Medical Imaging*, vol. 25, no. 6, pp. 701–711, 2006.

[35] M. A. Alnafea, K. Wells, M. Guy, and N. M. Spyrou, "Near field corrections for coded aperture imaging in scintimammography," in *IEEE Nuclear Science Symposium Conference Record*, vol. 5, 2006, pp. 2948–2953.

[36] Y.-W. Chen, "Heuristic tomographic reconstruction of coded aperture images," in *IEEE Instrumentation and Measurement Technology Conference Proceedings*, 2007, pp. 1–5.

[37] H. Lang, L. Liu, and Q. Yang, "Design of NRAs having higher aperture opening ratio and autocorrelation compression ratio by means of a global optimization method," *Optik*, vol. 118, pp. 491–494, 2007.

[38] H. Lang, L. Liu, and Q. Yang, "A novel method to design flexible URAs," *Journal of Optics A: Pure and Applied Optics*, vol. 9, pp. 502–505, 2007.

[39] R. Accorsi, L. Celentano, P. Laccetti, R. C. Lanza, M. Marotta, G. Mettivier, M. C. Montesi, G. Roberti, and P. Russo, "High-resolution ^{125}I small animal imaging with a coded aperture and a hybrid pixel detector," *IEEE Transactions on Nuclear Science*, vol. 55, no. 1, pp. 481–490, 2008.

[40] B. W. Miller, H. H. Barrett, L. R. Furenlid, H. B. Barber, and R. J. Hunter, "Recent advances in bazookaSPECT: real-time data processing and the development of a gamma-ray microscope," *Nuclear Instruments and Methods in Physics Research*, vol. A 591, pp. 272–275, 2008.

[41] L. A. Shepp and B. F. Logan, "The Fourier reconstruction of a head section," *IEEE Transactions on Nuclear Science*, vol. 21, pp. 21–43, 1974.

[42] L. J. Meng and D. K. Wehe, "A gamma ray imager using clustered non-redundant array coded aperture," in *IEEE Nuclear Science Symposium Conference Record*, vol. 2, 2003, pp. 763–766.

[43] R. Accorsi, "A 15-μm resolution imager for soft X-ray emitters," in *IEEE Nuclear Science Symposium Conference Record*, vol. 5, 2004, pp. 2975–2979.

[44] H. H. Barrett and W. C. J. Hunter, “Detectors for small-animal SPECT I: overview of technologies,” in *Small-animal SPECT imaging*, M. A. Kupinski and H. H. Barrett, Eds. Springer, 2005, ch. 2, pp. 9–48.

[45] L. R. Furenlid, Y.-C. Chen, and H. Kim, “SPECT imager design and data-acquisition systems,” in *Small-animal SPECT imaging*, M. A. Kupinski and H. H. Barrett, Eds. Springer, 2005, ch. 6, pp. 115–138.

[46] J. A. van Staden, H. du Raan, M. G. Lötter, A. van Aswegen, and C. P. Herbst, “Production of radioactive quality assurance phantoms using a standard inkjet printer,” *Physics in Medicine and Biology*, vol. 52, pp. 329–337, 2007.

[47] H. El-Ali, M. Ljungberg, S.-E. Strand, J. Palmer, L. Malmgren, and J. Nilsson, “Calibration of a radioactive ink-based stack phantom and its applications in nuclear medicine,” *Cancer Biotherapy and Radiopharmaceuticals*, vol. 18, no. 2, pp. 201–207, 2003.

[48] R. A. Serway, R. J. Beichner, and J. W. Jewett, Jr., *Physics for scientists and engineers with modern physics*, 5th ed. Philadelphia: Saunders College Publishing, 2000, ch. 35, pp. 1106–1130.

[49] Y. Choi, J.-Y. Koo, and N.-Y. Lee, “Image reconstruction using the wavelet transform for positron emission tomography,” *IEEE Transactions on Medical Imaging*, vol. 20, no. 11, pp. 1188–1193, 2001.